

# Algorithmen für die Bildaufteilung und Rauschunterdrückung in der OCT-Angiographie

DIPLOMARBEIT

zur Erlangung des akademischen Grades

**Diplom-Ingenieurin**

im Rahmen des Studiums

**Medizinische Informatik**

eingereicht von

**Mona Fakher**

Matrikelnummer 9926435

an der  
Fakultät für Informatik der Technischen Universität Wien

Betreuung

Betreuer: Ao.Univ.Prof. Dr. Martin Gröschl, Institut für Angewandte Physik, TU Wien

Betreuer: Ao.Univ.Prof. Dr. Rainer A. Leitgeb, Zentrum für Medizinische Physik und  
Biomedizinische Technik, Medizinische Universität Wien

Wien,

\_\_\_\_\_  
Mona Fakher

\_\_\_\_\_  
Martin Gröschl/ Rainer Leitgeb

# Image De-noising and Segmentation algorithms for OCT-Angiography

DIPLOMA THESIS

Submitted in partial fulfilment of the requirements for the degree of

**Diplom-Ingenieurin**

in

**Medizinische Informatik**

by

**Mona Fakher BSc.**

Registration Number 9926435

to the  
Faculty of Informatics at the Vienna University of Technology

Advising

Advisor: Prof. Dr. Martin Gröschl, PhD, Institute of Applied Physics, TU Wien

Advisor: Prof. Rainer A. Leitgeb, PhD, Center for Medical Physics and Biomedical  
Engineering, Medical University of Vienna

Vienna,

---

Mona Fakher

---

Martin Gröschl/ Rainer Leitgeb



# Erklärung zur Verfassung der Arbeit

Mona Fakher, Bakk.Techn.  
Grinzinger Str. 145/2/67, 1190 Wien

Hiermit erkläre ich, dass ich diese Arbeit selbstständig verfasst habe, dass ich die verwendeten Quellen und Hilfsmittel vollständig angegeben habe und dass ich die Stellen der Arbeit – einschließlich Tabellen, Karten und Abbildungen –, die anderen Werken oder dem Internet im Wortlaut oder dem Sinn nach entnommen sind, auf jeden Fall unter Angabe der Quelle als Entlehnung kenntlich gemacht habe.

Wien,

---

Mona Fakher

# Acknowledgements

At first, I would like to acknowledge Prof. Leitgeb of the Center for Medical Physics and Biomedical Engineering at Medical University of Vienna and Prof. Gröschl of Institute of Applied Physics at the Vienna University of Technology as my thesis advisors, who supervised me and I am gratefully indebted to their for their very valuable inputs and hints. Also for their moral support.

I would also like to express my deep gratitude to all the people that helped me in this project: DI Laurin Ginner, DI Marco Augustin. Thanks, for their support, guidance and patience for the success of this work.

Finally, I must express my very profound gratitude to my family for providing me with unfailing support and continuous encouragement throughout my years of study and through the process of researching and writing this thesis. This accomplishment would not have been possible without them. Thank you.

# Abstract

One of the most causes of blindness in the world, particularly in the elderly, is glaucoma [1]. The term "glaucoma" is a heterogeneous group of ocular diseases. Glaucoma is a disease that affects the optic nerve. The retina serves the function of light perception. For this, the light is absorbed by photoreceptors. The light pulses are converted into nerve signals and transmitted via the optic nerve; progressive damage of the optic nerve fibres leads to visual field defects with loss of visual function [2]. Early detection is one of the essential factors for preventing optic nerve damage and blindness caused by glaucoma. Periodic check-ups and early diagnosis of the disease can prevent blindness. If the treatment starts early enough, it is possible to avoid loss of vision. Periodic check-ups, including imaging systems like OCT and image analysis by experts, check for rapid changes in the pattern of blood vessels and the development of different changes in the retina. This examination method is very time consuming, expensive and requires qualified personnel. Automated systems for the detection of glaucoma are necessary. However, problems such as lack of good quality retinal images, prevent a completely automated screening system. This is because the elements of anatomy and lesions in the retina are not visible on the poor-quality images. Optical coherence tomography (OCT) has become the golden standard in ophthalmic imaging and diagnostics capable to acquire tissue volume data non-invasively and with high resolution close to the level of histopathology. An important functional extension of OCT is OCT-angiography (OCTA), which enables display of retinal microvasculature without need of injecting contrast agents. Those angiographic maps introduce novel and promising biomarkers for early disease diagnostics including glaucoma. OCTA is naturally co-registered with OCT, since the OCTA vascular contrast is calculated directly from the OCT intensity images. The main goal of this thesis, is to develop or improve a way of detecting glaucoma faster and earlier based on OCT images by applying advanced image processing methods. The aim of this work is to implement a segmentation algorithm for OCT angiography, which allows a proper extraction of different microvascular beds from the OCT tomogram. For the segmentation, the intensity tomogram is used to find the different retinal layers. This information will be transferred to the OCT angiography to extract the corresponding layers. Furthermore, a review of quantification and analysis of the de-noising algorithms for the OCT-angiography images will be performed. This should lead to the identification of biomarkers, based on the vascular structure for various eye diseases, which effect the micro vascular structure in the human eye.

# Kurzfassung

Eine der weltweit häufigsten Ursachen für Blindheit, insbesondere bei älteren Menschen, ist der Grüne Star (Glaukom). Der Begriff „Glaukom“ beschreibt eine heterogene Gruppe von Augenkrankheiten. Ein Glaukom ist eine Krankheit, die den Sehnerv schädigt. Die Netzhaut dient der Funktion der Lichtwahrnehmung. Hierzu wird das Licht von Fotorezeptoren absorbiert. Die Lichtimpulse werden in Nervensignale umgewandelt und über den Sehnerv übertragen. Eine fortschreitende Schädigung der Sehnervfasern führt zu Sehfeldstörungen mit Verlust der Sehfunktion. Eine Früherkennung ist einer der wesentlichen Faktoren um Sehnervschäden und durch Glaukom verursachte Blindheit zu vermeiden. Regelmäßige Kontrolluntersuchungen und eine Früherkennung der Krankheit können eine Erblindung verhindern. Wenn eine Behandlung früh genug beginnt, ist es möglich einen Sehverlust zu verhindern. Kontrolluntersuchungen umfassen bildgebende Systeme wie OCT und eine von Experten durchgeführte Bildanalyse, sowie eine Überprüfung auf Musterveränderungen der Blutgefäße und die Entstehung von verschiedenen Ablagerung in der Netzhaut. Diese Untersuchungsmethode ist sehr zeitaufwendig und teuer. Außerdem wird dafür qualifiziertes Personal benötigt. Automatisierte Systeme zur Glaukomerkenung wären wünschenswert. Allerdings verhindern Probleme wie das Fehlen von hochqualitativen Netzhautbildern, ein komplett automatisiertes Erkennungssystem. Dies weil die Elemente der Anatomie und Läsionen in der Netzhaut nicht auf Bildern mit schlechter Qualität erkennbar sind. Das Hauptziel dieser Diplomarbeit ist es einen Weg zu finden ein Glaukom schneller und früher durch eine auf Bildverarbeitung basierende Methode zu erkennen. Ziel dieser Arbeit ist es, einen Segmentierungsalgorithmus für die OCT-Angiographie zu implementieren, der eine korrekte Extraktion verschiedener Schichten innerhalb des OCT-Tomogramms ermöglicht. Für die Segmentierung wird das Intensitätstomogramm verwendet, um die verschiedenen Schichten der Netzhaut zu finden. Diese Informationen werden auf die OCT-Angiographie übertragen, um die entsprechenden Schichten zu extrahieren. Des Weiteren wird eine Quantifizierung und der Analyse des Rauschreduktionsalgorithmus für OCT-Angiographiebilder durchgeführt. Dies ermöglicht die Identifizierung von Biomarkern, die auf der Gefäßstruktur verschiedener Augenerkrankungen beruhen, welche die Mikrogefäßstruktur im menschlichen Auge verändern.

# Contents

<b>Erklärung zur Verfassung der Arbeit</b>	<b>i</b>
<b>Acknowledgements</b>	<b>ii</b>
<b>Abstract</b>	<b>iii</b>
<b>Kurzfassung</b>	<b>iv</b>
<b>Contents</b>	<b>v</b>
<b>1 Introduction</b>	<b>1</b>
1.1 Motivation	1
1.2 Aims and objectives	2
1.3 Outline of the thesis	3
<b>2 Background</b>	<b>5</b>
2.1 Eye	5
2.2 Physical structure of the eye	5
2.3 Eye diseases	9
2.3.1 <i>Glaucoma</i>	9
2.4 Diagnosis of glaucoma	11
<b>3 Optical methods</b>	<b>13</b>
3.1 Optic Coherence Tomography OCT	13
3.1.1 <i>Interferometric measuring principle of OCT</i>	15
3.1.2 <i>Time Domain OCT (TD-OCT)</i>	16
3.1.3 <i>Fourier Domain OCT (FD-OCT)</i>	16
3.1.4 <i>Spectral Domain OCT (SD-OCT)</i>	17
3.1.5 <i>Swept-Source-OCT (SS-OCT)</i>	17
3.1.6 <i>A-scan and B-scan image</i>	17
3.1.7 <i>OCT-Angiography</i>	18
3.2 A review of past research	18
<b>4 Methodology</b>	<b>22</b>
4.1 Image Processing Algorithm and analysis	22



4.2	Image recording system	23
4.3	Proposed segmentation method	24
4.4	Image segmentation	24
	4.4.1 <i>General description of the algorithm</i>	25
4.5	Layer detection	30
4.6	OCTA en-face Image De-noising	34
	4.6.1 <i>Fixed pattern noise</i>	35
	4.6.2 <i>Image pre-processing</i>	36
	4.6.3 <i>Image de-noising with median filter</i>	37
	4.6.4 <i>Histogram equalization</i>	39
	4.6.5 <i>Review of used noise removal techniques</i>	41
<b>5</b>	<b>Results and Conclusions</b>	<b>50</b>
	<b>Acronyms</b>	<b>52</b>
	<b>List of figures</b>	<b>54</b>
	<b>List of flowcharts</b>	<b>55</b>
	<b>Bibliography</b>	<b>56</b>



# 1 Introduction

A whole series of imaging procedures have been developed for scientific and medical use over the last century, covering individual areas. These range from X-ray diffraction analysis, to the determination of the structure of biomolecules and computer and magnetic resonance tomography for the representation of organisms. A special role for medical diagnostics is provided by methods that enable in vivo and on-site diagnostics of morphological structures of about  $\mu\text{m}$  to mm.

Among the advances in science and technology involving high computational efficiency, medical imaging is most obvious because of its high appeal in showing the structure of the human body. The techniques and methods are used for making images of the human body (or its parts and functions) for clinical purposes (medical methods that recognize, treat and examine diseases), or medical sciences (including anatomical and physiological studies). Medical imaging is a mixture of several branches of science, such as medical physics, medical technology, biology and optics [3].

Medical image processing has opened up a multitude of new possibilities for medical diagnostics and therapy. Innovations in the field of medical imaging provide new insights into the morphological, functional and molecular structure of the human body, with increased resolution, quality and accuracy. Through this development, computer support is becoming increasingly important in the evaluation and interpretation of complex image information.

At the Center for Medical Physics and Biomedical, Medical University of Vienna, a number of different methods of medical imaging system and image processing are researched and new methods are developed. This work is performed to the researches and investigations on OCT imaging system based on SS-OCT and image processing of OCT images in the Prof. Leitgeb-laboratory.

According to the research title, which is one of the important methods for the imaging and diagnosis of diseases based on medical images, it is necessary to explain the development of medical imaging of the eye.

## 1.1 Motivation

Medical imaging is in fact the technique and process used to create images of the human body (or parts and functions thereof), for clinical (medical procedures analysis, recognition and treatment of diseases) or medical (including anatomical and Physiological studies) purposes. Medical imaging is a combination of several branches of science, such as medical physics, medical engineering, biology, and optics.

Although no history of medical imaging has been written, one can still consider the role of physicists and engineers in a historical context. The first modern imaging technique and modality goes back to the discovery of X-rays by William Roentgen in 1895. However, the interesting thing is, that changes and improvements in imaging of diseases have been developed more due to the creativity of the laboratories, than by physicists and engineers. Various methods have been developed to capture selected obscured areas.

Therefore, radiologists when faced by the operational limitations of the devices they designed used different, sometimes invasive methods, to facilitate detection of invisible organs. From the early 1950s to the 1970s, a revolution took place in diagnostic imaging systems. New systems were developed for the non-invasive anatomical and functional imaging (disease

process). In this, physicists and engineers played a dominant role. The revolution began with nuclear imaging and ultrasound, which detected disease progression despite the serious limitations of the image. Until then, this had not been possible without these methods. Computer tomography was another field of medical imaging, introduced in the early 1970s. In this technique, good cross-sectional images were produced that provided the same information as from exploratory surgery. Devices were developed rapidly and standardized techniques were introduced for various methods. Revolutions and developments continued in the field of imaging. These developments are not limited to a profound improvement in existing systems, but also include the development of new imaging modalities. Different categories for medical imaging are presented, which are further categorized according to the origin of the image [3].

Similarly, various methods for the analysis and development of medical images, especially for eye diseases, were investigated and developed. One of the most important diagnostic tools in ophthalmology is optical coherence tomography (OCT). Alongside the further development of software systems and diagnostic techniques in diseases, this progress in the field of ophthalmology was also impressive. Its prototype is an OCT machine that vectorises different parts of the eye (cornea and retina). Until recent years, due to lack of this technology, there was very little information about many eye diseases, especially in the field of retinal diseases. But now, due this device, which is based on low-coherence interferometry, even the tissue and the cellular planes of the different layers of the eye, especially the retina, can be examined contact-free and with resolution close to the level of histopathology.

The aim of this study is to provide an automatic method based on the principles of image processing to ultimately support image based diagnosis of eye diseases in the retina [3]. The manual segmentation of layers of retina is very time consuming, complicated, and can lead to erroneous results. By an automated segmentation can save in the time and effort. An automated algorithm can provide better segmentation results than manual segmentation by experts. On the other hand, improving the quality of images can leads to better results. Therefore, the noise of images are also removed to achieve better results for the Feature Extraction.

## **1.2 Aims and objectives**

Several studies have been conducted in the field of medical signal processing. One of the most attractive areas in the signal processing of ophthalmic medical images, is to process medical images in the eye, obtained with OCT. As described above, OCT is one of the most popular visual imaging techniques among ophthalmologists, which helps them to diagnose and prevent many diseases. The great technological advantage of the OCT, apart from being contact-free as opposed to ultrasound imaging, is the decoupling of the depth resolution from the transverse resolution. Depth resolution is obtained through depth localized interference of the back-reflected sample light with an external reference beam. The result is virtually thin sections as used in microscopy, which allows images of microscopic images of living tissue (in vivo) to be taken. The high sensitivity detects very small signals (with light intensities below nW) and detects the specified depth structures with low input power. Therefore, this is a good way to study light-sensitive tissue. The use of OCT is limited in depth of the penetration by the electromagnetic wavelength-dependence of scattering within the object to be inspected, and the axial resolution is determined by the spectral bandwidth of the light source.

In this work, the segmentation of the retinal layers is aimed first. The goal of the segmentation is to achieve various aspects of the diagnosis of glaucoma as described below:

- The thickness of the retinal nerve fiber layer as the most important prognostic biomarker for glaucoma
- Assessment of the integrity of the capillary bed in the ganglion cell layer to detect the loss of ganglion cells earlier
- Segmentation of the inner retinal vessels against the choroidal vessels can identify signs of proliferative age-related macular degeneration when identifying abnormal vessel growth from the choroid to the retina

In this research, we are also trying to resolve the important problem of noise reduction, with the help of previous research, in view of the urgent need for doctors to be able to use this technology for improved diagnosis.

The OCT uses a movement contrast to image the blood flow and thereby image the vasculature. Therefore, occurrence of artifacts are more common and may affect the OCTA images. These artifacts are due to various reasons such as patient movement due to heartbeats, trigger issues of OCT systems or scanner synchronization errors and may lead to a wrong interpretation of OCT angiography images. To prepare the image data for better quality and efficient feature extraction, the artifacts are reduced in OCTA en-face images [4].

The practical part of this work is explained as follows:

- OCT intensity image pre-processing to obtain the data in correct structure
- Layer segmentation to extract the features of the retina within tomograms
- Applying the segmentation to OCTA tomograms to extract specific microvascular beds
- Noise reduction on OCTA en-face projections to prepare the data for further feature extraction

### 1.3 Outline of the thesis

This thesis is structured as follows:

**Chapter 1:** describes the research question and the objective of this project.

**Chapter 2:** describes the physical structure of the human eye, the retinal layers, and their functions

**Chapter 3:** describes the optical methods and different retinal imaging techniques and presents an overview of past research into different methods used for retina segmentation.

**Chapter 4:** describes the image processing and the implemented algorithms.

**Chapter 5:** provides results and discussion.

**Chapter 6:** gives conclusions.



# 2 Background

## 2.1 Eye

The eye is the most important sensory organ. Only with the help of the eye, we are able to recognize images. More specifically, the eye perceives visual stimuli from outside and transforms them into electrical impulses. Subsequently, the information is passed on to the brain through the optic nerve.

The following section describes the parts or components of the eye and their functions, and the next section will illustrate the most common eye diseases, such as glaucoma and diabetic eye disease.

## 2.2 Physical structure of the eye

The components of the eye and their functions are briefly described in the following section.

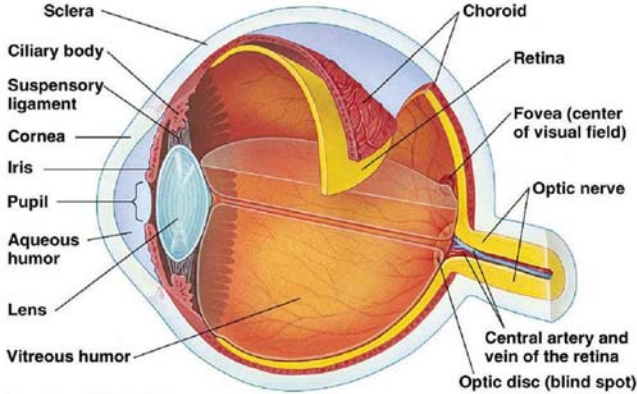


Figure 1: Human Eye Structure [5]

A cross-section of a human eye is presented in Figure 1.

As the light comes into the eye, it first comes into contact with the cornea. The task of the cornea is to filter the light and direct it, so that the image can converge in the eye following the path of the iris and pupil. By narrowing or dilating, the iris adjusts the pupil size to regulate the amount of light that can enter the eye. With the help of auxiliary muscles, the lens can change its shape and focus on objects, it also improves the already refined image from the cornea and projects it onto the retina [6].

Eye components	Function
Sclera	Maintains shape of eye; protects eyeball; site of eye muscle attachment
Eyelids	Eye protection

Cornea	Refracts incoming light; focuses light on the retina
Iris	Regulates amount of incoming light
Pupil	Admits light
Lens	Refracts and focuses light rays using accommodation
Aqueous humor	Helps maintain shape of eye; maintains intraocular pressure; nourishes and cushions cornea and lens
Vitreous humor	Maintains intraocular pressure; transmits light to retina; keeps retina firmly pressed against choroids
Choroid	Absorbs stray light; nourishes retina
Retina	Absorbs light; stores vitamin A; forms impulses which are transmitted to brain
Optic nerve	Transmits impulses to the brain

**Table 1: Eye components and functions**

The most important parts which are considered in this study are the retina, choroid and optic nerve, which are explained in detail in the following section:

**Choroid:**

The choroid is one of the layers of the eye that lies between the sclera and the retina. This granular layer contains many capillaries that feed the iris and retinal light receptor cells. This layer is located below the retina pigmented epithelium or RPE [7]. Several diseases, such as choroidal polyps, choroidal tumours, age-related degeneration, capillary arteriosclerotic changes and hereditary diseases of the retina, change the structure of this layer, so the separation of this layer is important [8, 9, 10]. There are a limited number of non-invasive techniques for examining the choroid. Today, the methods for evaluating the choroid are the carotid ultrasound, magnetic imaging and histological studies [11, 12]. Contact ultrasonic can produce an internal image of the choroid, but the accuracy of the image is low, and accurate measurement of the position is difficult. Imaging of the choroid using an OCT device is challenging due to the difficulty of transmitting the signal through the RPE layer and increasing the depth of imaging. With spectrometer, based 800nm OCT an enhanced depth imaging mode has been introduced (EDI-OCT) to better visualise the choroid layers [13]. With the rise of swept source OCT at 1060nm center wavelength, the choroid can now be better visualized as opposed to 800nm center wavelength and became the focus of many studies [14].

Because a large amount of information is contained in such images, it is not possible for the ophthalmologist to analyse this data without a automatically system and over-dimensioned. However, because of the heterogeneity in the choroid layers, the methods previously used in segmentation of the retina layers are not suitable for the heterogeneous structure of choroid layers. In several studies, EDI-OCT was used to measure the thickness of the choroid to examine the association with retinal diseases and to consider the treatment process [15].



In this research, swept source OCT at 1060nm is used, and measurements are based on manual labelling, which is a lengthy and time-consuming process. This is a particularly acute problem when the number of people to be examined is high. Kajic et al. designed a two-step statistical model that automatically finds the layers of the choroid in the OCT images recorded at 1060nm in a healthy and diseased eye [16]. However, the model requires extensive training. In 2012, an automatic method for measuring the thickness of the choroid was introduced by Tian et al., by finding the shortest path of the graph, which was used on 10 images to check their efficiency. But this method needed much more data. Regarding what has been said about making EDI-OCT a useful medical tool, the need for the development and improvement of the automatic segmentation algorithm is required.

### Retina:

Retinal tissue is a multilayer structure that contains multiple layers including the posterior part of the eye cavity and is responsible for the transformation of the light energy into neuronal signals for final analysis by the brain [17].

The retina can be divided into many distinguishable layers as shown in Figure 2.

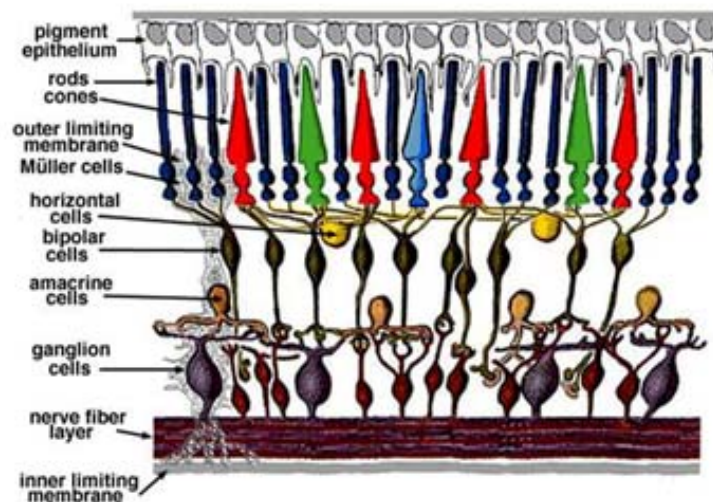


**Figure 2: Different layers of retina**

“The different layers of retina are organized as follows [18]:

1. The Inner Limiting Membrane (ILM) is the boundary between vitreous body and the retina.
2. Ganglion Cell Layer (GCL) encompasses the cell bodies and axons of the ganglion cells.
3. Inner Plexiform Layer (IPL) comprises the synapses between bipolar, amacrine, and ganglion cells.
4. Inner Nuclear Layer (INL) involves bipolar cell, horizontal and amacrine cell bodies.
5. Outer Plexiform Layer (OPL) consists of bipolar cells, horizontal and receptor synapses.
6. Outer Nuclear Layer (ONL) contains the nuclei of photoreceptor.

7. Outer Limiting Membrane (OLM) comes into contact with the base of the inner segments of photoreceptor.
8. Photoreceptor Layer contains the inner and outer segments of photoreceptors.
9. The Pigment Epithelium Layer is the outermost layer of the retina be composed of pigmented cuboidal cells that contain Melanin. Melanin is the black pigment, which absorbs any excess light that is not captured by the retina and prevents it from reflection back to the retina. Thus, protects the photoreceptors from damaging level of light. The pigment epithelium cells provide nutrition such as glucose, and essential ions to photoreceptors.”

Two of the most important retinal diseases are glaucoma and diabetic retinopathy [19]. A detailed examination of the retina for the recognition of these diseases requires a detailed representation of the layers of the retina. Since the eighteenth century, a large number of imaging devices such as x-ray imaging and MRI have been essential tools in the field of medicine and biology. However, tomography machines have problems, such as high prices, aggressiveness of ionizing radiation and low resolution. Therefore, to eliminate these problems, many researchers have introduced optical coherence imaging or OCT. This optical technology creates two-dimensional or three-dimensional images with high resolution of anatomical tissues [20].

An early diagnosis of these diseases provides a good opportunity for treating these diseases. An early diagnosis of early-stage disease is difficult for a number of reasons:

- Sensitivity of the field-of-view test for detecting damage
- Insufficient sensitivity of imaging tools for detecting structural changes
- Variable measurable parameters in persons requiring diagnosis [21].
- Motion artifacts during in-vivo assessment due to involuntary eye motion, fixation loss, or heart beat.

Because most organs in the body are symmetrical, asymmetry analysis can help physicians to diagnose diseases earlier and faster. The limit of the asymmetry parameters is a good measure for the early diagnosis of diseases. One of their applications is asymmetry analysis in the diagnosis of cancers, such as breast cancer, in its early stages [22]. In addition, asymmetry analyse is used in the brain hemisphere to identify people with multiple sclerosis or the early stages of psychosis and in the diagnosis of eye diseases. In 2005, asymmetrical analysis data about the thickness of the retinal neural fibre layer was obtained comparing the left and right eyes of healthy people in the area of the optical disc. However, it should be noted that the asymmetry limit was not calculated in this research [23]. Subsequently, the posterior pole symmetry analysis was used to detect early glaucoma. This study was limited to one layer and the asymmetric threshold was not calculated [21]. The asymmetric analysis examined the thickness of the nerve fibre between the left and right eyes of healthy people. This study was limited to the retinal nerve fibre layer [24].

In the macula region, there are several layers of ganglion cells, even if only one layer of the cells remains due to the disease, the visual field test is normal (i.e. with the loss of five of these cell layers, about 30 micrometres, it is still within normal limits). It should be considered that healthy people have many variations in the thickness and as a result, of the change from the cup to the disc ratio [21]. Asymmetry analysis of the total thickness of the retina in the macula region can help physicians to diagnose the disease at an earlier stage. Therefore, achieving a threshold for thickness change could be an important step in this direction.

## Optic nerve:

For the complete transmission of the visual information from the retina to the opticum brain, the visual tract that begins in the retina and runs above the optic nerve, optic chiasm, optic tract, lateral geniculate nucleus and optic radiation to the visual cortex are needed. The optic nerve is the only structure of the central nervous system, which can be directly visualized clinically. It represents the accumulation of ganglion cell axons, which converge on the optic disc. Both optic nerves end in the optic chiasma, which again has the optic tract as posteroventral origin. More than a million neurons, arranged together in a series of strands, form the optic nerve. The optic nerve, fixes the retina, to the brain like a thin, light-sensitive screen in the back of the spinal cord. For good vision, a healthy nerve is essential [25].

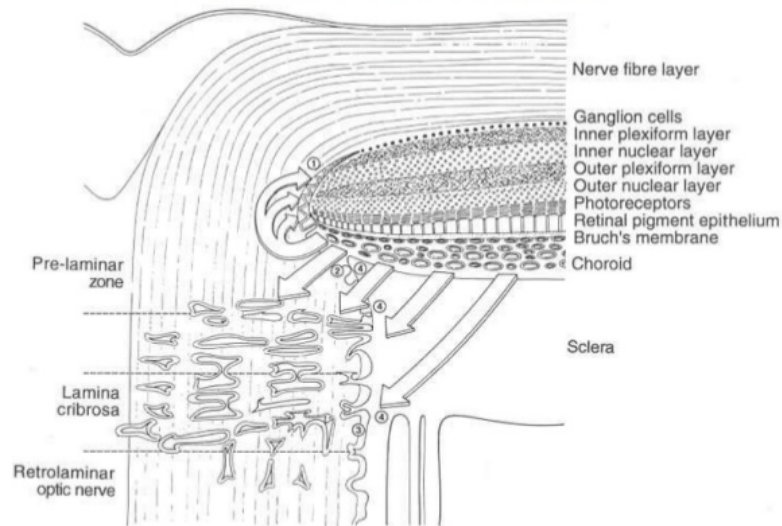


Figure 3: Parts of Optic Nerve [26]

## 2.3 Eye diseases

Blurred vision, floaters, flashes, spots, light sensitivity, these are frequent eye problems that cause discomfort and are the primary symptoms of eye disease. The eye has many diseases. Each of them has its own way of being identified, investigated and prevented. Currently, glaucoma is one of the most important diseases in the eye.

They will be explained in the following section:

### 2.3.1 Glaucoma

Glaucoma is a chronic degeneration of the nerve plexus. An example of it is vascular neuropathy. Patients with this particular type of glaucoma lose their peripheral vision and if they are not treated, can lose vision completely [27]. The types of glaucoma are: open angle, closed angle and advanced types, which are themselves classified into primary and secondary types. The most important clinical characteristics of primary open-angle glaucoma are cup-shaped optic nerves combined with visual field loss. Although high intraocular pressure cannot be considered as a clinical feature of this disease, there are indications that black race, old

age, family history of glaucoma, angioedema, short-sightedness and low diastolic pressure are risk factors for primary open glaucoma [28].

The term "glaucoma" refers to a group of diseases that can affect the visual acuity and cause loss of the visual field. Nerve damage dependent on glaucoma is associated with a progressive decrease in the axons of retinal ganglion cells (RGC) and also with the reformation of two optic nerve head and troughs optic disc [29]. Two basic hypotheses which were described by the pathology of this disease, are the mechanical hypothesis and the vascular hypothesis (ischemic) [30]. The mechanical hypothesis asserts the importance of direct compression of the axons and supporting structures of the front of the optic nerve, as well as the leaf of lamina scapular and break of axoplasmic flow, which leads to the death of RGC. The vascular hypothesis (ischemic) affirms the development of neuronal anaemia and thus the reduction of perinatal nerve perfusion. This reduction in blood flow can be due to the effect of intraocular pressure on the optic nerve with effects on the processes of the optic nerve [29].

### 2.3.1.1 Effect of glaucoma on the optic nerve

Many factors are responsible for the development of glaucoma. Increased intraocular pressure is the most important risk factor for glaucoma damage, in addition to a disturbed blood flow to the optic nerve. A certain pressure in the interior of the eye is necessary so that the eye retains its spherical shape. The so-called aqueous humour is responsible for maintaining the pressure. This is a clear fluid circulating in the anterior eye segment between the cornea, iris and lens. The aqueous humour is formed in the ciliary body, which is located behind the iris. Through a fine canal system (trabecular meshwork), it can be transported out of the eye after a certain time. In the healthy eye, there is a balance between production and outflow of the aqueous humour, which leads to a relatively constant eye pressure. This equilibrium may be disturbed in glaucoma. Either too much aqueous humour is produced or too little chamber fluid flows out because the drain path is clogged. The eye pressure rises. The creeping pressure increase over months and years at first causes no symptoms. Due to the constantly increased pressure on the optic nerve, however, depending on its pressure sensitivity, there may be a slow, progressive decrease in visual performance. The patient does not notice this for a long time.

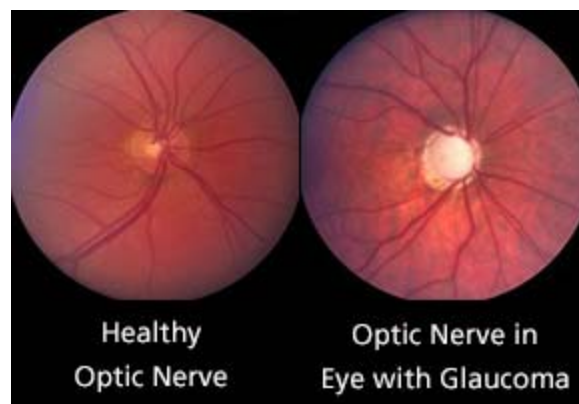


Figure 4: Healthy Optic Nerve and with Glaucoma [31]

## 2.4 Diagnosis of glaucoma

Many people think that they are only affected by glaucoma if they have high pressure in their eyes. But this is not always the case. The high pressure in the eye increases the risk of glaucoma. Nevertheless, this is not an unconditional cause of this disease. The risk of glaucoma due to high pressure in the eye depends on the amount of high pressure that the optic nerve can withstand and this varies from person to person. The normal pressure is generally between 12 and 21 mm Hg, but also at this pressure, a person may have anaemia, which indicates that the eye examination is very important.

Regular examinations by the ophthalmologist are therefore important. The patients' individual pressure sensitivity plays an important role in the development of glaucoma. Some patients react to relatively low intraocular pressure values with glaucoma damage, while others do not develop glaucoma even at much higher-pressure levels. Up to now, an eye pressure between 10 and 21 mmHg was considered normal. In recent years, however, only about 50 percent of open-angle glaucoma cases have been diagnosed by eye pressure, and only about 1/3 of patients with a pressure of 20-30 mmHg develop glaucoma damage. Furthermore, 30-50% of patients with typical visual defects have an intraocular pressure below 21 mmHg [32].

The following image shows an example of this disease.



**Figure 5: Normal Vision and with Glaucoma [33]**

There are several tests for the detection of glaucoma such as:

- Manometer: Pressure measurement
- Gonioscopy: Evaluating the internal drainage system of the eye
- Ophthalmoscopy: looking at the retina and optic nerve head
- Perimeter: Visual field testing [34]

A Goldmann tonometer provides the golden standard for the measurement of intraocular pressure [35].



### 3 Optical methods

The word “light” in engineering sciences is often used for the visible spectrum, infrared and ultraviolet. Because light is an electromagnetic wave, it shows a similar behaviour to other electromagnetic waves (like X-ray, microwave). Near-infrared-spectrum -emitters and -lasers are one of the most widely used resources in this imaging technique.

The theory of optical imaging is based on the absorption of photons by the elements in the human body. Through various mechanism and events, higher resolution images are produced to display the different parts of the body. Because the resolution depends especially on the spectral bandwidth of the light source.

Significant optical absorbers in the human body are oxygenated-haemoglobin (oxyhaemoglobin) and deoxygenated haemoglobin (haemoglobin). In addition, there are other absorbers in most tissues, such as melanin and water, which have absorption at visible and near infrared wavelengths. The maximum penetration of light into the tissue can be achieved in a certain area where the absorption and scattering of light through tissue is at least. This area is called “optical window”, which is shown in Figure 6 for the absorption and scattering of light by haemoglobin and water. [36]

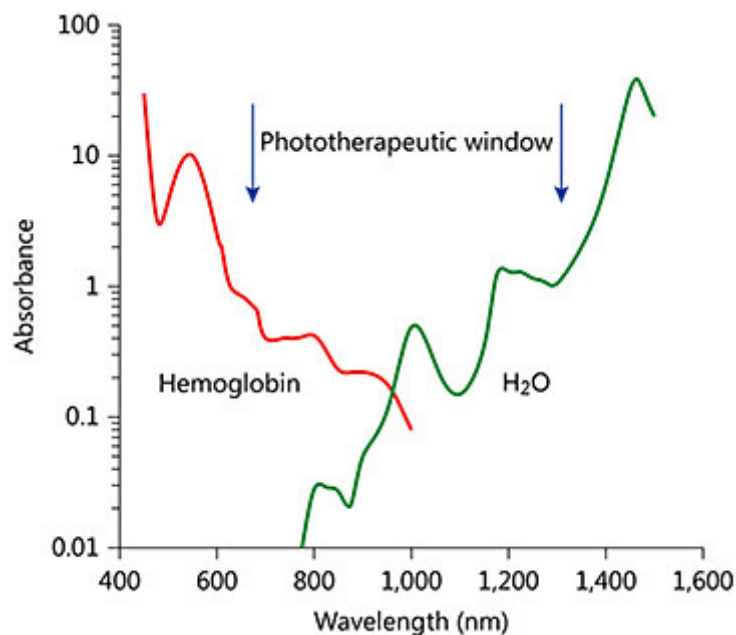
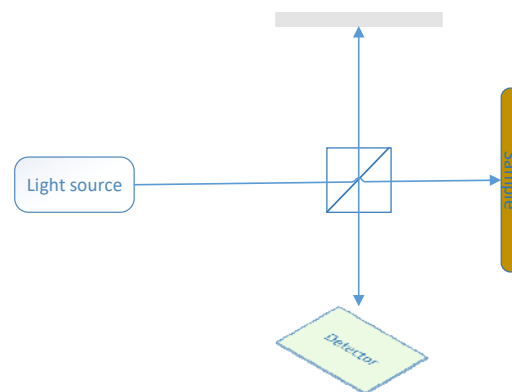


Figure 6: Tissue optical window (Water, Hb) [36]

#### 3.1 Optic Coherence Tomography OCT

As currently defined, tomography is a method to extract the maximum information required from the environment in depth. This extracted information may be a two-dimensional in depth or three-dimensional image of the targeted environment. The extraction of information takes place by the processing of raw data, which is derived from the boundaries of the object. Angiographic systems are mainly used for the contrasting of body tissues vasculature in

medicine. Angiography systems, such as OCTA, are expensively used in medical imaging, especially in ophthalmology and retinal imaging with a high resolution of about  $10\mu\text{m}$  [37]. The measurement and imaging of surface morphology, including optical surfaces, etc, is very important in science and engineering and is an essential tool in production. Interferometric systems are one of the effective methods for measuring various levels of profiles [38]. One of the important problems of measurement in interferometric systems is the relatively high sensitivity of the system to motion and noise.



**Figure 7: Michelson's Interferometry**

Optical coherence tomography (OCT) has revolutionized the representation of retinal structures and the diagnosis of pathological changes in the fundus of the eye in recent years. Before the introduction of OCT, no in-vivo representation of the layer structure of the retina was possible. In principle, three-dimensional imaging is faced with the challenge of not only imaging surfaces, but also assigning the image information to a depth or preventing the superposition of images or scattered radiation from different depths. Light cut illumination, e.g. used in the slit lamp, uses different directions between illumination and observation for depth selection. Confocal microscopy forms a focal point in the tissue on a matched aperture to eliminate blurred images from higher and lower layers. In both methods, the lateral resolution depends on the angular range that can be used for imaging. When the retina is imaged, the usable angular range is limited by the iris. In the case of imaging methods, which, as in the case of ultrasound diagnostics, evaluate wave propagation times, the depth resolution is independent of the focusing angle. Ultimately, the OCT also uses run-time measurements to achieve the depth resolution required for a three-dimensional retina display [39]. Today, OCT systems have a depth resolution in the range of  $1 - 10 \mu\text{m}$ , and it is possible to make images of the sample in real-time in situ and in vivo. The position of the OCT with regard to other medical imaging systems is shown in the diagram "Resolution depth of the penetration" in Figure 8.



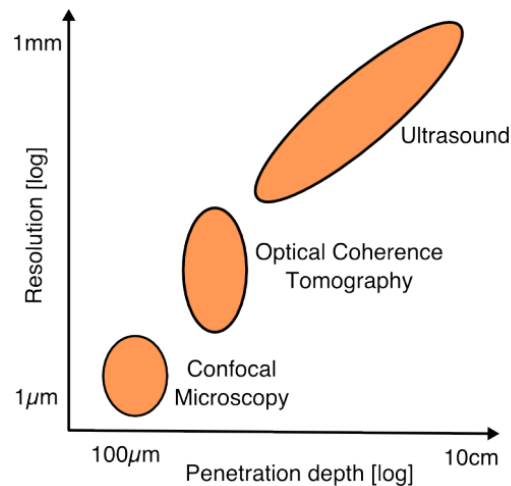


**Figure 8: Resolution depth of the penetration**

OCT is based on the physical phenomenon of white light interferometry and detects small refractive index differences within the sample. The light, which is used for OCT imaging, is used instead of the audio signal in ultrasound imaging, and the image formation depends on the optical properties of the tissue structure. Due to the high speed of light, a direct measurement of the echo signal delay is not possible. For this reason, OCT systems work based on interferometry with low coherence. Typical light sources with low temporal coherence are super-luminescence diodes or femtosecond lasers, which have very short pulses. In OCT imaging, light is irradiating the sample and the backscattered light is superimposed to a reference beam using an interferometer. The contrast in the tissue originates from scattering processes at structural boundaries, which represent a transition in the optical refractive index, e.g. the transition from tissue to cell (cell membrane) or the transition from cell plasma to mitochondria. Light is also scattered at such scattering centres, to a small extent, exactly opposite to the direction of incidence. In order to allow light to penetrate so far into the tissue at all, a wavelength, which is in the near infrared range of 800 nm-1350 nm, is preferably selected. The average free path length between two scattering processes in optically opaque fabrics lies in this wavelength range, in the order of magnitude of a few 100 μm up to millimetres. The absorption by water or other tissue absorbers is less severe than the losses due to scattering. The transparent part of the eye (cornea, pre-chamber, lens, glass body) can be completely captured, the relatively thin and complex layer of the retina is also very impressive.

### 3.1.1 Interferometric measuring principle of OCT

The light of a spectrally broadband light source is divided in amplitude. One part traverses the optical path of a reference arm, the other part is applied to the sample and reflected back from there. Both parts are superimposed at the exit of the interferometer. The reference light and the sample light interfere with each other if the relative path length matches to within the short temporal coherence length. The interferometric evaluation can be realized in various ways. Two fundamental types can be distinguished: Time Domain OCT and Spectral Domain OCT. One of the important problems of measurement in interferometric systems is the relatively high sensitivity of the system to motion and noise [40].

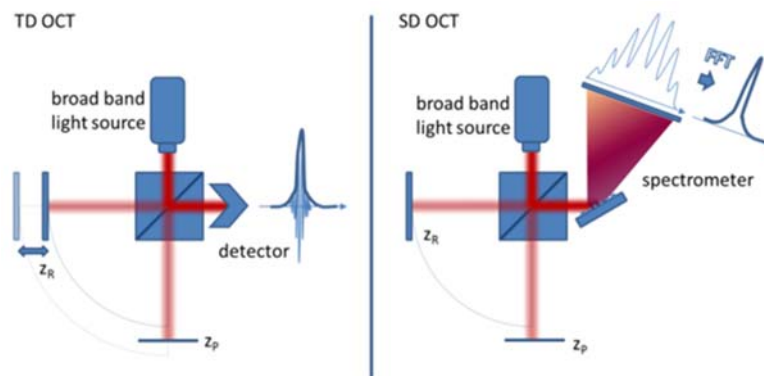


Figure 9: TD-OCT and SD-OCT

### 3.1.2 Time Domain OCT (TD-OCT)

The light of the two arms is temporally correlated with each other. For this purpose, the reference arm is shifted in length and the runtime in this arm is thus changed. If the running time corresponds to the running time of a reflection from the sample, the reference arm wave and sample arm wave are in phase and the electric field strengths are added for all the wavelengths contained in the spectrum. Even a distortion of the arms of half the central shaft length causes a mutual extinction. A further shift causes constructive interference. The further one is from the exact coordination of the path lengths, the flatter the expression of the waves and valleys is - the interference contrast decreases. This is because there is a different distance between the central interference maxima and the next minimum for each wavelength contained, and, of course, the electric field strength of all wavelengths is added up at each point. The more wavelengths are contained, the more the interference amplitude decreases by the exact tuning point. The  $1/e^2$  width of the envelopes of the interferogram is the temporal coherence length of the light. It is inversely proportional to the spectral bandwidth of the light source. However, exactly the envelope is the decisive measurement value of the OCT and is obtained from the interferogram by a filtering method. The course of these envelopes in a multilayer sample results in a depth profile of the sample, also called A-scan. Measuring several A-scans at successive lateral points comprises then an OCT tomogram or B-scan [41].

### 3.1.3 Fourier Domain OCT (FD-OCT)

OCT systems of the 4th generation measure with a non-movable reference mirror using the Fourier transformation. This measuring principle is referred to as Frequency Domain or Spectral-domain OCT. In the case of the Fourier Domain OCT, the light paths from and to the eye, as well as to the reference mirror, are like the time domain. However, the reference mirror is fixed after positioning.

The interference is evaluated spectrally, i.e. the superimposition of the reference arm light and the sample light is evaluated at each wavelength. This can be done by means of a downstream spectrometer or by temporally spectrally determined laser light sources (Swept Source OCT). In both cases, the spectroscopic interferogram is recalculated to wave numbers and Fourier transformed. The Fourier transform of the power spectrum with respect to wavenumber

translates the spectral coordinate to the adjoint temporal or depth coordinate. Thus, an A-scan is again obtained from the spectrum and again the axial resolution is inversely proportional to the spectral bandwidth of the light source. In addition, there is the finite resolution of the spectrometer or the instantaneous line width of the tuned laser. They have an effect on the possible measuring depth range. The finer the spectrometer resolution or the instantaneous laser linewidth of the swept laser, and the smaller the possible distance between the sampling points in the spectrum is, the measuring range is larger. Overall, the retinal layers can be better represented in the FD-OCT systems due to the faster acquisition and the resulting higher lateral sampling. However, retinal diseases strongly affect the visibility of different layers or their configuration, e.g. in CNV (Choroidal Neovascularization) or retinal oedema the structure is disturbed to such an extent that the reflection behaviour becomes untypical and thus the corresponding layer can no longer be recognized. The volume representation of the FD-OCT systems usually allows scrolling through the scans in the form of a small film retrospectively, whereby viewing from different positions is possible. This allows a rapid qualitative assessment of the retinal structures [42].

#### **3.1.4 Spectral Domain OCT (SD-OCT)**

The reference arm is fixed slightly longer or longer than the sample arm. The two waves from the sample and reference arm are combined, interfere and are then directed to a spectrometer. This is equipped with a diffraction grating. As a result, the wave packets are spatially separated according to their optical frequencies and the spectral interference pattern is then registered by a CCD detector. After reading the individual CCD cells, further processing by ADC converters and Fourier transform (FT), the known A-scan is again obtained as in TD-OCT [41].

#### **3.1.5 Swept-Source-OCT (SS-OCT)**

Another method also measuring in the Fourier domain, is the so-called SweptSource (SS) - OCT. Instead of a broadband light source, a monochromatic light source is used, the wavelength of which can be changed periodically over a certain range. The intensity at the output of the interferometer is detected with a photodiode. The difference to spectral domain OCT is that this is now no longer spatially resolved with spectrometer, but the spectral interference pattern is recorded over time. A spectral decomposition with a monochromator is therefore not necessary. This makes the construction of the system much easier. At the same time, the complexity of the light source increases. While simple semiconductor light sources are used in the spectral radar, the SSOCT requires a complex laser light source. Their properties also define the essential characteristics of the complete OCT system [43].

#### **3.1.6 A-scan and B-scan image**

If the sample is scanned with a light beam, a depth profile along the light beam for each screen point is obtained either by scanning the reference arm mirror as in TD-OCT or by Fourier transform of the spectral interference pattern as in FD-OCT. The corresponding representation of a depth profile is called the amplitude scan (A-scan). The conversion of the depth profile into brightness and the representation of many adjacent depth profiles along a screen path as brightness values, results in a tomogram or so-called brightness mode image (B-Scan). If two layers are close to each other, they can still be resolved if their distance in depth is greater than the coherence length of the light. The transverse resolving power depends on the focusing of the light beam. The shorter the focal distance is, the more accurate is the resolution in the focal plane; but the best resolution decreases with increasing distance in front of and behind this selected focal plane according to Gaussian beam optics.

According to Gaussian optics the lateral spot size is given as where  $\lambda$  is the central wavelength,  $f$  is the focal length, and  $d$  is the beam waist diameter at the focusing lens. The confocal range, being the range of optimal lateral resolution, is related to the lateral spot size as . Obviously the better the lateral resolution the worse the confocal depth range. A compromise is to use low lateral resolution or spot size, which in retinal imaging is usually about 10  $\mu\text{m}$ -20  $\mu\text{m}$  in diameter. If the focus spot size is about 1 $\mu\text{m}$  and less, you are no longer talking about OCT but of optical coherence microscopy [41].

### **3.1.7 OCT-Angiography**

OCT-angiography (OCTA) is a novel, non-invasive imaging technique that enables imaging of different retinal and choroidal vascular networks with high resolution, based on motion contrasts. It allows visualization of the microperfusion of retinal and choroidal vessels without the use of an intravenously administered dye. This enables an examination of vascular changes in retinal diseases at the time of diagnosis and under therapy process. The OCTA allows precise, three-dimensional visualization, whereby leakage, pooling and staining phenomena or inflow behaviour is not detectable [44].

OCTA utilizes a high OCT scanning speed and performs repeated scans at the same location, and then identifies blood vessels by detecting red blood cell flow. In this way, OCTA can be used to construct a 3D dataset to represent the vascular portion of the scanned tissue and automated or semi-automated segmentation boundaries. Accurate depth segmentation of the structural tomogram provides efficient evaluation of retinal and choroidal vasculature to differentiate between healthy and diseased retinas [45] [46].

#### **3.1.7.1 Clinical applications of OCTA**

Optical Coherence Tomography (OCT) is a success story in the scientific and technological field. The spatial resolution of 3 microns or even less, allows the tissues to be studied almost at the cellular level. OCT is an invaluable assistant in the diagnosis of many diseases of the anterior and posterior segments of the eye. OCT has revolutionized the sensitivity and specificity of diagnosis, tracking and response to treatment in almost all areas of clinical practice with primary eye pathologies and secondary eye features in systemic disorders such as diabetes mellitus, hypertension, vascular and neurological disorders. OCT is proven to be a helpful tool for the early diagnosis of diseases of the eye, such as glaucoma and retinopathies caused by early changes in the morphology of the retina and especially of the nerve fibre layer [47].

The application fields for OCTA are diverse and include, a. neovascular age-dependent macular degeneration (AMD), diabetic retinopathy, retinal vascular occlusions, inflammatory diseases and telangiectasia of various aetiology. The results of the imaging and their interpretation are, in part, different from those of classical fluorescein and indocyanine green angiography. Knowledge of these differences as well as limitations of the method of investigation, are important for clinical application and interpretation [48].

## **3.2 A review of past research**

In 2016, Huang, together with his colleagues, conducted a study on the investigation of dynamic imaging by using an OCT angiography method of retinal imaging. The purpose of this research was to finally provide a solution for patients by preventing chronic ocular diseases. In this study, they responded to the problems of eye pressure measurement by OCT

angiography and Doppler. In this research, the Doppler values are corrected based on the angle extracted from the OCT and a 3D- algorithm or -method based on dynamic programming, is proposed to extract the 3D boundaries of the veins. The accuracy of blood pressure, which was diagnosed with pressure phantoms, was examined, and is confirmed by the proposed method [49].

In another study, conducted in 2016, the aim of the study was to provide a method for researching and working on eye tumours in patients. In fact, the problem of noise reduction for OCT angiography images was presented. Finally, the research was presented for removing noise from angiographic images used to identify and detect ocular tumours. In this research, the accuracy of the presented results is reliable [50].

Liu, along with other colleagues, in an interesting study which was completed in 2015, used OCT images to investigate CNV. In fact, the determination and detection of the CNV area is very important. This paper presents an automatic method for the detection of the CNV region. The results of this study were compared with the results from the manual diagnosis of CNV. The results of the automatic examinations were adequate and precise [51].

In 2015, Varga and colleagues, presented a study of OCT images from MS patients. The aim of this study was to identify anatomical difference and achieve visualization of the retina layer in patients with MS, as well as assessing the utility of neurological changes with OCT image segmentation [52]. In this study, the proposed method was used on 38 patients with MS, who were evaluated by OCT. The method presented in this study uses image processing techniques to extract the desired texture using OCTRIMA software. The OCTRIMA software enables the segmentation of the various cellular layers of the retina. The results obtained in this study were also confirmed by laboratory tests on the patients. But the main target of this study was to find a solution for identifying patients with MS by using OCT images.

Tang, along with other colleagues in 2017, presented a study of diabetics, based on OCT images. Damaged capillaries were studied in diabetics. Capillary tissue was damaged by many factors. In this study, 434 patients were examined. The main outcome of the study, based on OCT images, was a solution for the treatment of diabetics [53].

In 2017, Munk has proposed a quality survey of four OCT imaging techniques [54]. The purpose of this research is to provide a way to review or research study series in this field. The purpose of this research, is to identify and investigate OCT image processing methods in a way that is based on the devices referred to in this research, such as through trials, and finally, result in the introduction of a method.

Huang Huang with his colleagues in 2016, conducted a study on the determination of the CNV area, based on OCT images. The main problem faced by the researchers in this study was the question of noise-reduction of OCT images used to determine the CNV region [55].

Yang, together with his colleagues in 2014, published a study about the recording of OCT images or adaptation of the OCT images. In fact, the main problem addressed by these researchers was eye movement during imaging. The solution proposed in this study is a two-part solution using a comparison stabilizer for the optical component and the digital images. In this study, the mirror is slowly reflected by two axes to stabilize and adjust the images. One of the most important results of this study was the reduction of eye movements due to the use of the stabilizer, which was improved about 10-15 times [56].

Zaki with his colleagues in a study of 2017, has researched the removal of noise from OCT images. In this research, the relationship between the signal detection of noise spectra is

determined to eliminate the noise in the OCT images, based on the width of the violet thresholds, which clearly results in the noise removal, in particular in the case of sharp noise. The proposed method in this research is based on noise reduction by using the violet method [57].

Jahromi and his colleagues also conducted a study on the segmentation of OCT images in 2017. In the study, researchers found that corneal disease has a direct correlation with the measurement and calculation of corneal thickness in several layers. Although precise segmentation of corneal borders is unavoidable, manual measurement is time consuming and inaccurate. In this research, the Gaussian mixed model is presented for the automation of the segmentation of the three important parts of the corneal horn skin based on OCT images. The method proposed for this research, presented by Jahromi and colleagues, is based on two parts. First, the GMM (Gaussian mixed model) is used on the original images for the purpose of locating the beginning and end of the boundaries. Ultimately, the test will be performed to determine the exact secondary border. The proposed method was compared with the boundaries identified using the manual extraction method which showed that the results presented from the researched automated method were reliable and promising [58].

In 2016 the problem of noise due to moving patients was investigated in a study by Lezama and colleagues. In fact, such noise is detected in situations where the visual field is too large. One of the best ways to overcome this problem is to make images in 2 vertical vectors. However, the image matching in this situation is very complicated, with long-term data transmission and noise. In practice, the gap between the imaging and the eye movement, as well as the fast movement of the eyes while focusing, does not provide us with proper information, so the problem of image matching is critically examined. In this research, researchers have approached the problem of OCT image adaptation in the process of automatically correcting the patient's eye movement. Their proposed method is also performed when the patient has a retinal detachment. The results presented in this study clearly demonstrate that the proposed method has a good ability to deliver results [59].

In 2016, Dascal also presented an overview of OCT images. In this study, the application of the proposed method was based on X-ray images. In the method proposed in this paper, image adjustment of vascular tree patterns is illustrated on x-ray images. The same method would also apply to OCT images [60].

In 2017 Baghaie introduced a study together with other colleagues. In this study, the method proposed was for avoiding noise caused by eye movement, on OCT images. In this study, noise reduction techniques are divided into two parts because of the eye movements [61].

- Methods based on hardware-related techniques
- Methods based on software techniques.



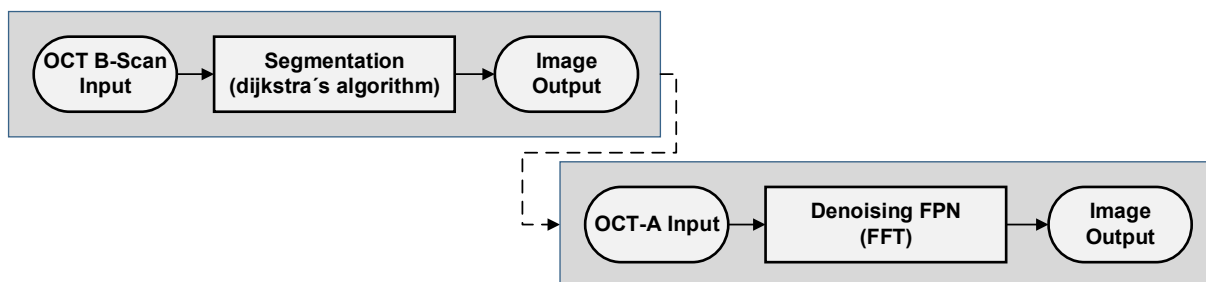
## 4 Methodology

This practical part of this work is divided into two different parts. First, the OCT B-scan images are segmented. Secondly, the OCT angiography images are denoised.

The proposed method for the segmentation is based on the graph theory approach to automatically segment the different retina layers on the OCT B-Scan images.

The second algorithm is also implemented to reduce the noise in the angiography input images. After trying different methods for the noise reduction, the Fixed-pattern noise (FPN) method was chosen.

Flowchart 1 below, briefly presents the general methodology.



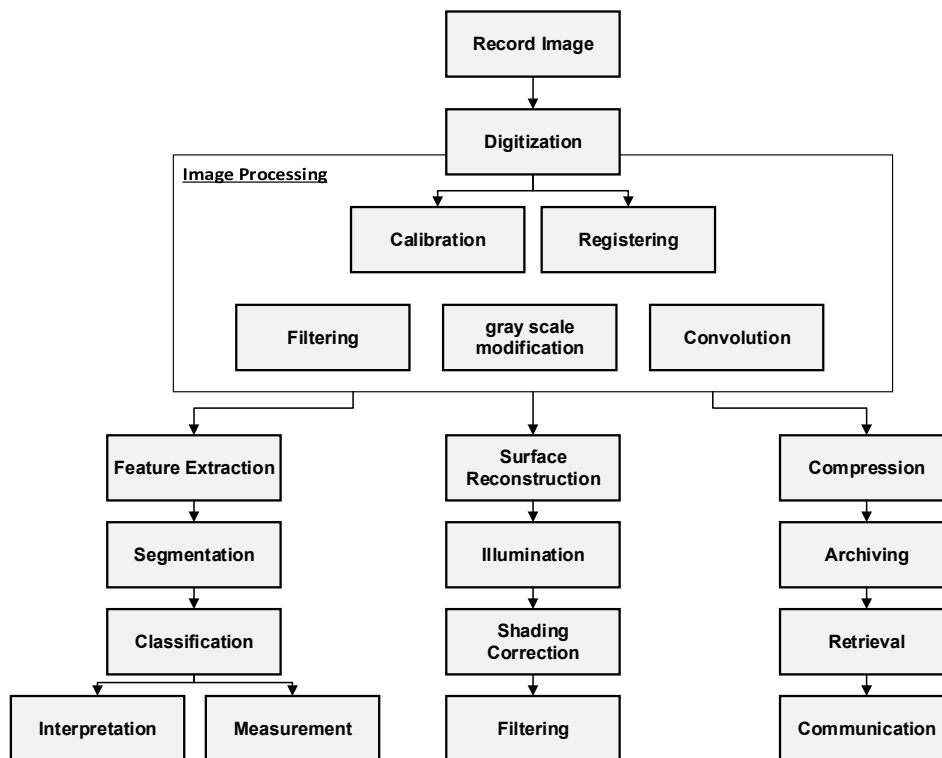
**Flowchart 1: General methodology**

A detailed explanation of the algorithms is given in Section 4.3. for segmentation, and in 4.4. for noise-reduction.

### 4.1 Image Processing Algorithm and analysis

Digital images consist of individual pixels (picture elements) with discrete brightness or colour values. They can be efficiently processed and objectively evaluated. This opens the door to an entire spectrum of methods of digital image processing in medicine. The current term "medical image processing" thus means the availability of digital image processing for medicine. Medical image processing also includes four large areas Flowchart 2. Image capture includes all steps from capture to the digital image matrix. Image representation includes all manipulations on this matrix, which are used for the optimized output of the image. Sub-image storage can be used to sum up all the techniques used for the efficient communication, archiving and retrieval of the data [3].





**Flowchart 2: Stages of the medical image processing [62]**

The important tasks of diagnosis and therapy-supporting image processing systems consist of the largely automated segmentation, analysis, identification and visualization of medical image objects (tissue, tumours, lesions, vascular systems, etc.). The development and design of such image processing systems is characterized by the integration of algorithms, methods and techniques from the fields of medical image registration, segmentation, image analysis, pattern recognition, visualization and virtual reality [63].

## 4.2 Image recording system

Generally, image processing systems consist of a recording unit, e.g. a camera, an image memory, devices and methods for manipulating / processing the information and presentation devices for output.

The dataset that we have used in this work and have processed with the proposed algorithm, was recorded with a device, which was built for research in the field of OCT at the Centre for Medical Physics and Biomedical Engineering at the Medical University of Vienna. The image dataset is anonymized and used for research purposes.

A brief overview of how this device is constructed is given here:

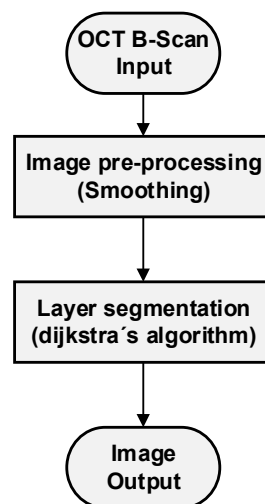
The system is based on the generally available swept-source technology. This system has been further developed to speed up the OCT-Angiography system. Two interleaved sources of laser are used. Each of these sources operates at 100 kHz and a total of 200 kHz is achieved. The split spectrum was developed by Ginner et al [64] and works specifically for swept source OCT by lateral scanning during wavelength sweep. Each lateral point sees only

part of the spectrum. By using this approach, doubling the FOV from 8 ° (100 kHz) to 16 ° (400 kHz) is achieved without increasing the recording time.

### 4.3 Proposed segmentation method

The method used to segment the SS-OCT B-Scan images is based on the method proposed by Chiu et al. [65]. This method automatically extracts and differentiates the different layered structures of the retina. It is based on graph theory and dynamic programming to reduce the processing time for segmenting and extracting features.

In the flowchart below, the general steps for the implementation of the segmentation algorithm are shown, which are described in detail in the following sub-sections.



Flowchart 3: Segmentation general steps

### 4.4 Image segmentation

The purpose of this section is the separation and segmentation of images (OCT-B-Scan). There are already many methods that have been used for the segmentation process of the retina. The main purpose of this section is to perform the segmentation, which is shown in Figure 10 automatically.

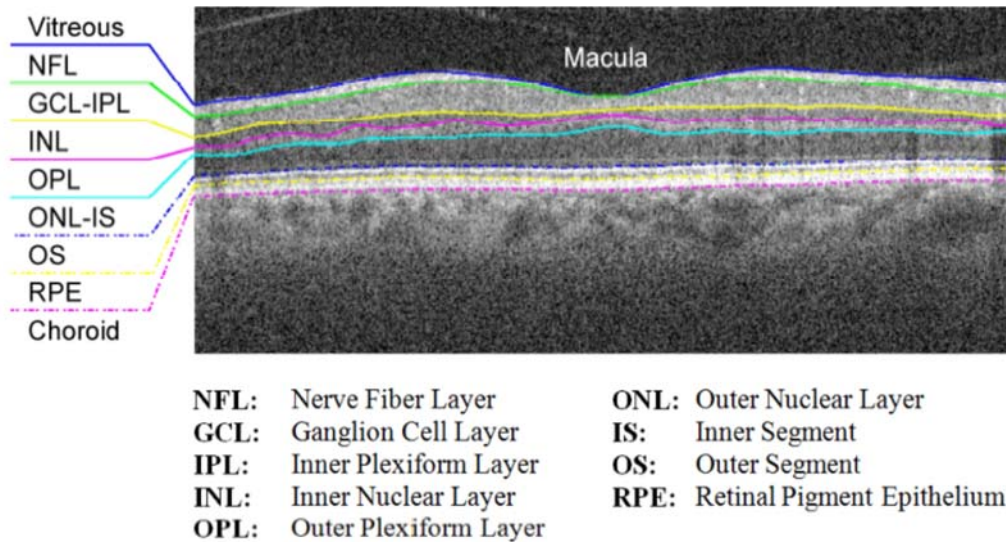
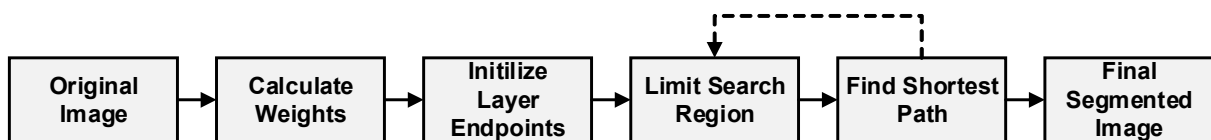


Figure 10: Target retinal layers of a cross-sectional SD-OCT image (B-scan) centered at the macula [65]

#### 4.4.1 General description of the algorithm

The general steps for implementing the algorithm are as follows:



Flowchart 4: Segmentation algorithm

First, the graph weights must be calculated. Here the gradient of image is used because each pixel of the image is a node on the graph. The connection between two nodes are the edges. A path consists of a set of connected edges and only pixels (nodes) with 8 adjacent paths are considered. In other words, distant pixels (outside the neighbourhood) have a weight equal to infinity and no access to each other. Thus, the number of graph nodes is equal to the number of pixels in each image, and the nodes in the neighbourhood are edges and connected.

Figure 11 shows an example of three connected nodes. For the search for minimally weighted path with Dijkstra's algorithm, the weights must be both positive and between  $\{0,1\}$ . An edge-weight of zero indicates an unconnected node pair. The table of graph weights is an adjacency matrix. One axis represents the start node and the other axis represents the end node.

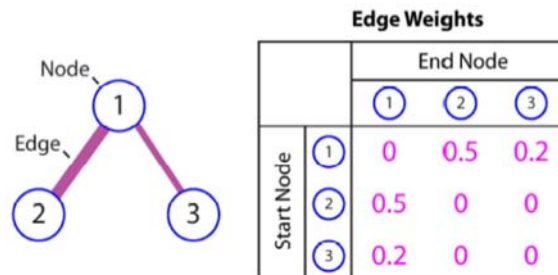


Figure 11: Example graph weights (adjacency matrix) [65]

To passing from a start node to an end node, the path with the minimum weight is preferred. These paths are in fact the borders/ boundaries between the areas. The weight between the two neighbouring pixels is correlated with the gradient of the two pixels and the gradient is normalized between  $\{0,1\}$ .

$$(1) w_{ab} = 2 - (g_a + g_b) + w_{min}$$

- $w_{ab}$  is the weight assigned to the edge connecting nodes a and b,
- $g_a$  is the vertical gradient of the image at node a,
- $g_b$  is the vertical gradient of the image at node b,
- $w_{min}$  is the minimum weight in the graph, a small positive number added for system stabilization.

Where  $g$  represents the gradient of each pixel. Note that two graphs are made to identify areas. One graph is obtained using the absolute magnitude of the negative numbers of the gradient image and to find areas that change from light-to-dark (such as the border between the choroid region and the RPE) and the second graph is constructed from the positive numbers of the gradient and is suitable for locating regions where the dark-to-light transition occurs (like the NFL region).

In the next section of the algorithm, to avoid manual selection of start- and endnodes, we use an automatic initialization method to select the start and end nodes. In the Dijkstra-routing-algorithm, a node as the start point, and a node as the end node are given to the algorithm, and the output is the best and the least weighty path between the two nodes. Here, after adding two columns with the lowest value (closest to zero) to the sides of the image, pixel  $(1, 1)$  is given as the starting point and the last image pixel (right bottom) as the end point to the Dijkstra's algorithm.

The following Figure 12 shows an example of this automatic initialization technique. Two vertical columns with the least amount added to the sides of the image [65]. In addition, the start-and-end-points in the upper left and lower right corners are initialized. The edges are used as a function of pixel intensity. The darker pixels result in a lower weight. The red route shows the path with the lowest weight or the highest gradient value.



- If this is the case, the cost of this node is reduced to the new value. Otherwise, it is checked for another condition if the nodes are not yet been visited. If so, it will be added to the queue, so that edges that go away from this node can be later considered. In addition, this node has the cost resulting from the sum of the costs to its predecessor node and the cost of the newly discovered edge to itself.
- Nodes are selected from this queue until there are no more nodes in the queue. Then, the algorithm is finished and has found already from the start-node to all other nodes the lowest weight path [66].

Here is an example of a Dijkstra's algorithm for a graph with five nodes [67]:

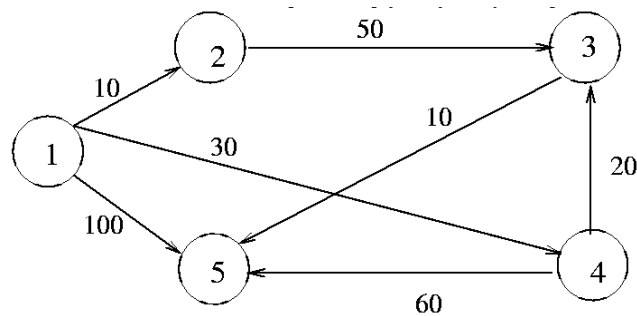


Figure 13: A graph example for Dijkstra's algorithm

Initially:

$S = \{1\}$ ,  $D[2] = 10$ ,  $D[3] = \infty$ ,  $D[4] = 30$ ,  $D[5] = 100$

Iteration 1:

Select  $w = 2$ , so that  $S = \{1, 2\}$

$D[3] = \min(\infty, D[2] + C[2, 3]) = 60$

$D[4] = \min(30, D[2] + C[2, 4]) = 30$

$D[5] = \min(100, D[2] + C[2, 5]) = 100$

Iteration 2:

Select  $w = 4$ , so that  $S = \{1, 2, 4\}$

$D[3] = \min(60, D[4] + C[4, 3]) = 50$

$D[5] = \min(100, D[4] + C[4, 5]) = 90$

Iteration 3:

Select  $w = 3$ , so that  $S = \{1, 2, 4, 3\}$

$D[5] = \min(90, D[3] + C[3, 5]) = 60$

Iteration 4:

Select  $w = 5$ , so that  $S = \{1, 2, 4, 3, 5\}$

$D[2] = 10$

$D[3] = 50$

$D[4] = 30$

$D[5] = 60$

This algorithm is a relatively greedy method with a relatively high time requirement. In this project, since the number of image pixels (graph nodes) is high, the time needed to find each path will inevitably be too long. However, since the direction of the path is usually from the left of the image to the right (depending on the starting point and the end point), we can prevent movements in the wrong direction, which leads to an increase in the speed of the algorithm. Also, to reduce the processing time, since our path is largely uncomplicated and has a less curve, we can examine only  $n$  (about 1000) of newly added nodes to the queue and the last weight and the next path to one of these  $n$  nodes is selected. This also increases the speed. An example of Input-Image is shown in Figure 14. All the steps of these algorithms, which are shown in this thesis as figures, are processes on this Input-image.

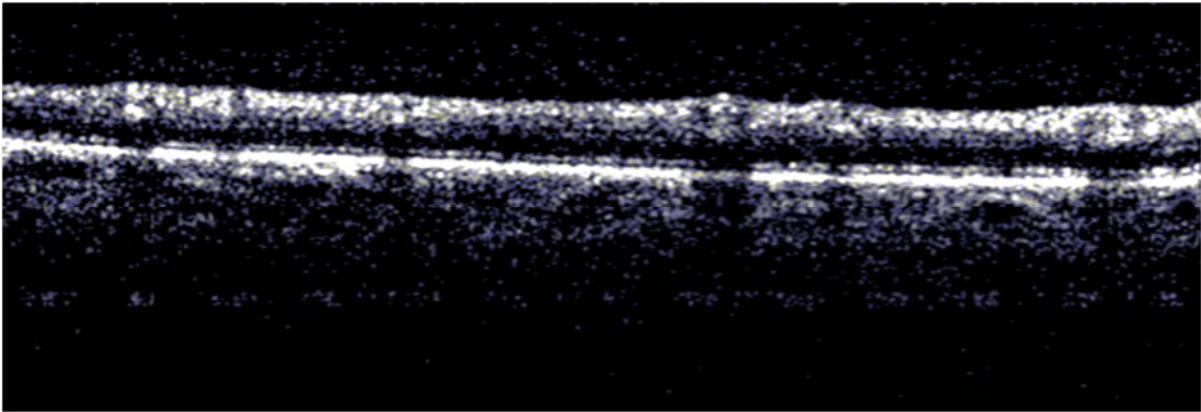
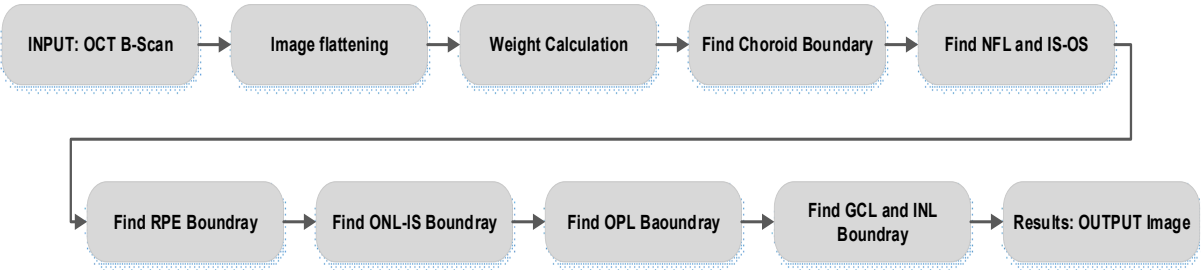


Figure 14: Input Image

**4.4.1.2 Implementation and details of the algorithm**

The details for implementing the algorithm are as follows:



Flowchart 5: Detailed segmentation algorithm

Pre-Processing/ Smoothing the boundaries of areas in the image

In this thesis, it is assumed that the RPE region has the highest brightness in each column of the image. Therefore, we can find the location of each pixel with the highest brightness, and assign it to the RPE as shown in Figure 15, witch smoothed with a Gaussian filter. The kernel size that we are using here is a 3x3 kernel.

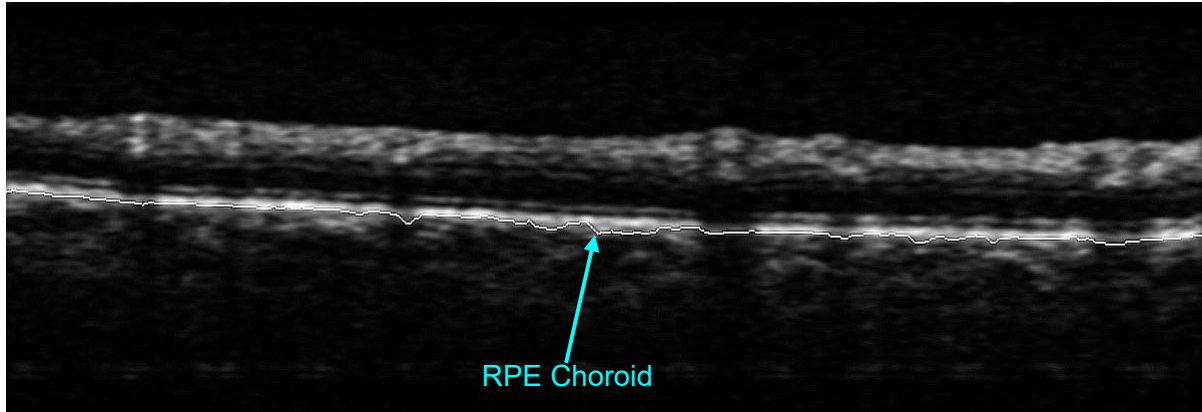


**Figure 15: RPE Boundary**

Then the deviated data is removed from the points and a second-degree curve is fitted to the rest of the data. In the next step, it is assumed that the node is a constant and the remaining points in each column are shifted downward as far as its height difference with the parabolic space. In this way, each column will have different motions.

#### Graph weight calculation

At this point, two graphs having the number of nodes equal to the number of pixels in the original image, plus the number of two pixels added to the sides of the image, are generated. For this purpose, the image is smoothed with a median filter. Then gradients are determined in the y-direction and the values obtained are normalized with thresholds to  $\{1, 1\}$ . The numbers in interval  $\{1, 0\}$  are used to construct the dark-to-light graph to find the boundaries of areas that change from darkness to the brightness, and numbers in the range  $\{0, 1\}$  to get the light-to-dark graph and to find the boundaries of the areas that change from brightness to darkness (such as the boundary between the RPE and the choroid).

It has to be considered that each node has eight edges equal to  $w_{ab} = 2 - (g_a + g_b) + w_{min}$ , and  $g_a$  and  $g_b$  are the gradients of the two nodes  $a, b$ . The starting point is always the top left of the image and the end point is the bottom right of the image. So, in the first and last two columns, only vertical movement is allowed, and other movements will surely dissipate the Dijkstra's algorithm. Therefore, the weight at the edges for the nodes in the first and second columns, is set so that only vertical movement (i.e. downward) is allowed.

### **4.5 Layer detection**

#### Finding the boundary of Choroid and IS OS, NFL

As already mentioned, regions with a clear border can easily be distinguished. So, we start by finding these borders. First, the boundary between the choroid and RPE is found by using the light-to-dark graph and the Dijkstra's algorithm, and with it, the approximate location of the RPE. Because the approximate height of the RPE is known, the starting point in the first column can be adjusted to ensure that the movement in the first and last nodes goes vertically and straight down. The resulting path can only be the boundary between the RPE and the choroid. The resulting choroid is indicated in the Figure 16 (obtained border is recognized as choroid).



Then the boundary between the ONL-IS and the OS (called the 'ONL-IS boundary') is located and the boundary between NFL and the vitreous (called the 'NFL') is located by using the light-to-dark graph.

Since the choroid border has already been calculated, the search can be restricted, because it is already known that there is no range below the choroid border. First, the NFL border is determined. To ensure that the boundary is the NFL, the weight of the graph edges in nodes that are lower than the (choroid border minus 30) pixels is maximized. It is known that the ONL-IS margin is less than 30 pixels (based on the basic data and the size of the images) from the Choroid boundary, it is determined that the path being extracted is the NFL boundary (this is the limit of the strongest gradient in the image, in the transition from darkness to brightness). After finding the NFL, the search range for the ONL-IS boundary can also be reduced (for example, to the range between the choroid edge and 50 pixels above the choroid). This limit is also obtained by using the dark-to-light graph and the Dijkstra's algorithm, as shown in Figure 16.

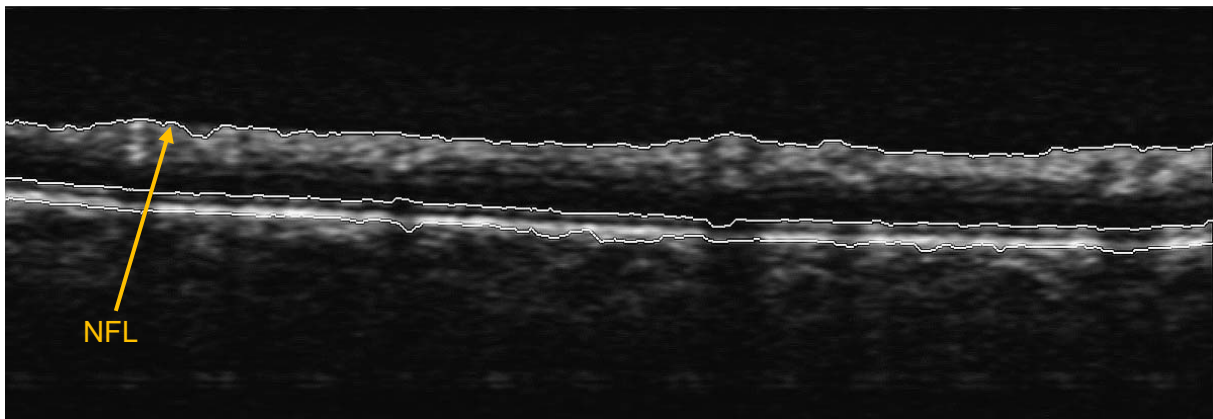


**Figure 16: NFL boundaries**

#### Finding the boundary of OS and RPE

To find the boundary between the RPE and OS (known as RPE), the dark-to-light diagram is used. Finding this limit is restricted to the choroid and ONL-IS boundaries, which have less range and are easily accessible. To limit the search location, as already mentioned, the graph weights outside of range are set to the maximum.

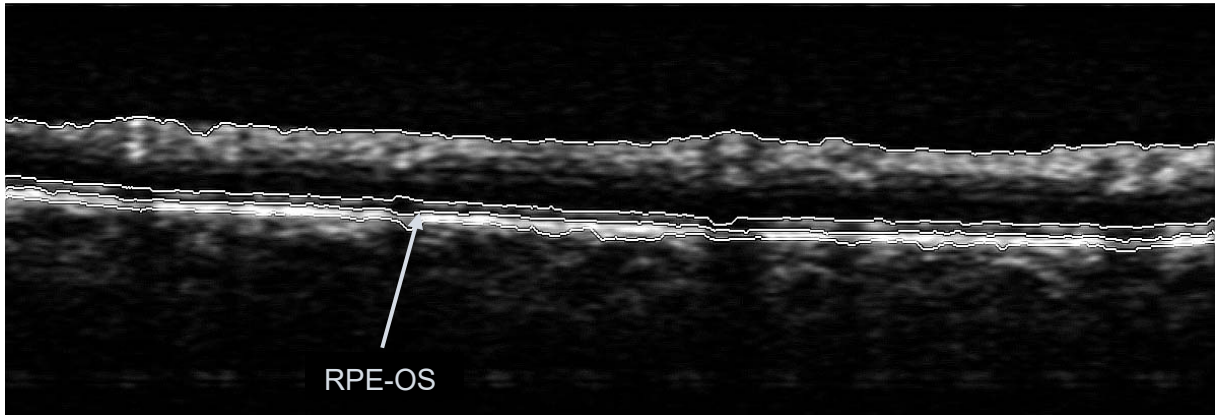


**Figure 17: RPE OS boundaries**

### Finding other boundaries

In this paper, to find the location of the remaining areas, one attempt to find the approximate location of each region, and then, by limiting the search areas, identify them exactly by starting at the borders of the previously calculated graphs and using the Dijkstra's algorithm. To do this, the image is first smoothed in the x-direction with a Median filter with 5 x 5 kernel size and the pixels that are less bright than the median is set to zero in each column. From the image obtained, the second derivative is taken in each column [68]. Then, a pilot binary mask is generated by thresholding the edge-enhanced image at zero. All non-null clusters that are less than 5 pixels tall will be set to zero and join the remaining clusters that are closer than 3 pixels from each other to remove the outliers in each column. Then, from that obtained image, parts with less than 500 pixels are removed, thereby giving a binary image with nearly separate boundaries for each region. Then, in each column from top to bottom, a number and colour is given for each part. Each colour gives the approximate location of an area.

After finding the approximately location of layers, extraction of the exact location of the other boundaries can begin. But the output image is not always in the same form and there are areas where there is a lot of curves or discontinuity. In this paper, in which an algorithm was used to segment the regions, a set of morphological operations were used to overcome and greatly reduce this problem. But in practice, these morphological operations (e.g. erode, dilate, opening, closing process) are not the same for each image, and different operations are required for different images. These steps were performed on our data, and it was observed that this part of the process poses many problems with different images.

To solve this problem, because the boundary between NFL and IS\_OS has already been found, a derivation from the original image within the remaining regions and normalization is performed again. Since the remaining regions do not have a clear boundary, the normalization of the gradient has to be more precise (with a lower threshold), so that these boundaries are also observed somewhere in the gradient image. So, in these areas, the weight of the graphs is recalculated and the graph weight is maximized for areas outside the range.

Beyond the IS\_OS border is the ONL-IS, which is almost the darkest area of all. Thus, the boundary between ONL-IS and OPL (the boundary named ONL-IS) can be found by using the light-to-dark graph. To ensure that the boundary is the same as the ONL-IS, the gradient image

in the pixels closest to IS\_OS, which themselves have a certain gradient, is increased again (e.g., twice). Then Dijkstra's algorithm is applied to the newly calculated graph for this range and the resulting output path is the same as the ONL-IS limit. See the Figure 18 below.

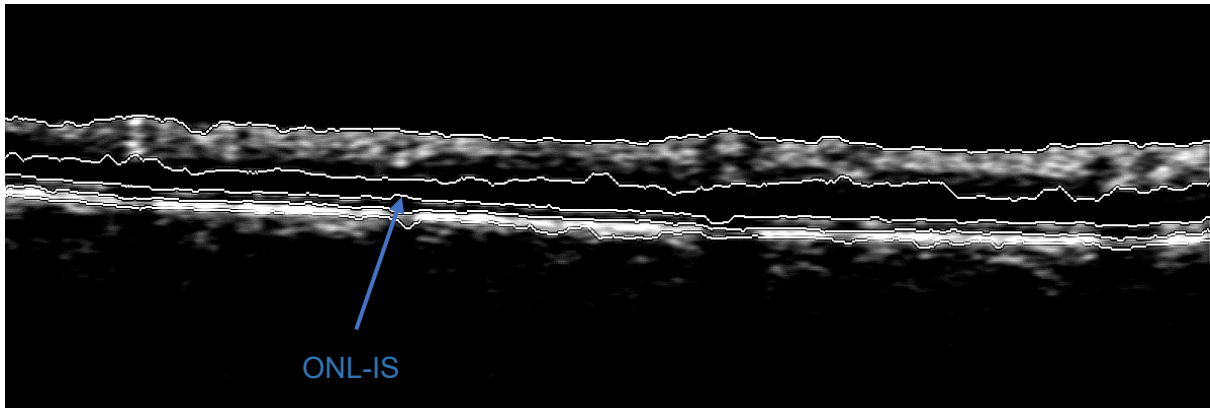


**Figure 18: ONL-IS boundary**

To find the boundary of the OPL (the boundary between the INL and OPL lines), the range is again limited to the NFL and the ONL-IS limit.

The search for this border begins with the help of the dark-to-light graph, which is recalculated for this area. This border is the only border between the remaining areas where there is a change from dark to light and it is one of the hardest boundaries to find because the boundaries are usually not quite clear, especially in our database and therefore the border found for this area is less accurate.

Now there are only two remaining boundaries and the search range is more limited. These two borders are INL (the boundary between INL and GCL) and GCL (the boundary between the GCL and NFL regions) and they are located by using the light-to-dark graph.

First, the GCL boundary is found. This limit is close to the NFL border and the brightness of the NFL area is always greater than the brightness of the other areas. By using these two properties, the approximate location of the GCL boundary is identified. Then, the gradient of the image at this boundary is increased, to ensure that the output of the Dijkstra's algorithm is that boundary. After finding the GCL, it will be easy to find the INL because the search area is very limited and there is only one more boundary with a strong gradient.

Finally, the two-dimensional image with the five founded layers, as shown in Figure 19.

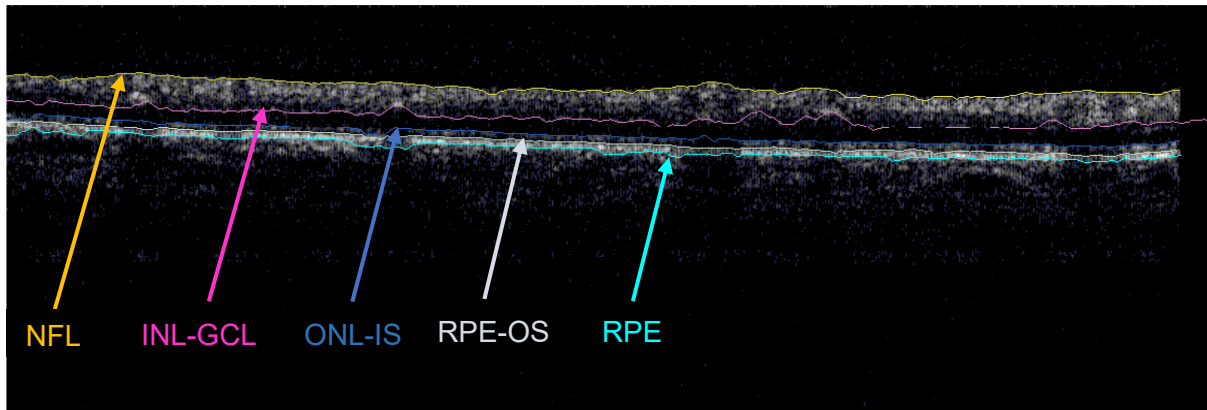


**Figure 19: Segmented image**

Note that the overall accuracy of the algorithm is dependent on the image itself (the contrast between the regions) as well as the values of the threshold levels for normalizing the gradient image.

The results show that this algorithm works. The processing time is high, but this can be reduced by GPU acceleration.

Indeed, this segmentation algorithm can identify layers of interest. These found layers are then applied to the OCTA movement contrast volumes to extract the vascular beds.

OCTA calculates maximum intensity projections to produce OCTA-En-face images. These en-face images often suffer from noise mainly due to motion artifacts, as well as slight synchronization errors of scanner driving with the detection system. Those artefacts appear typically as lines [4].

In the following section, an algorithm is developed to reduce the noise in OCTA images to get better image quality for the segmentation, which could make the layers better and easier to extract, therefore, solving the problem by reducing the FPN noise was attempted.

#### **4.6 OCTA en-face Image De-noising**

First, we will briefly explain about noise in imaging systems and afterwards we will consider different solutions for noise-reduction to find best technique.

##### **Noise:**

An unwanted factor with a low amplitude, high frequency (it repeats over a given time period), and which, when measured (e.g., in imaging), enters the system. The noise types can be distinguished into general noise due to the sensor electronics and noise specific for the image processing.

- Noise from optics
- Noise from the detector
- Noise during imaging due to external sources
- Noise from electricity spikes
- Noise due to unwanted patient bulk motion for motion contrasting
- Noise due to trigger synchronization errors for motion contrasting

The main source of noise in OCTA images is from unwanted patient motion and trigger synchronization. In this research, we attempt using one of the best methods or filters. The artefacts appear in the en-face OCTA images as stripes distributed along the slow scanning direction. Hence, this noise can be described as fixed pattern noise. First, a brief explanation is given about fixed pattern noise and the different filters, which we used to eliminate the noise, then the frequency filter will be considered, and finally we will explain the proposed method, which is the Fast Fourier Transformation filter.

#### 4.6.1 Fixed pattern noise

Fixed pattern noise appears in image sensors such as CCD cameras or CMOS cameras. The response of different pixels in a detector is not always the same for the same radiation. This is due to different noise sources in the detector. For example, the radiation  $I$  on the pixel  $m$  will lead to output  $O_m$  and the same radiation on the pixel  $n$  to output  $O_n$ . The difference in the response of different pixels leads to the generation of a fixed pattern, in the form of noise in the image [69]. This problem, especially in medical images, could lead to incorrect diagnosis and it can even change the form of complications. The fixed pattern noise in CMOS and CCD sensors is shown in Figure 20.

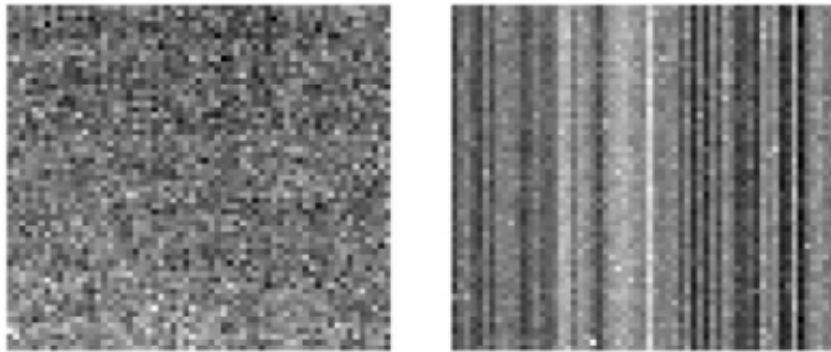


Figure 20: Effect of fixed pattern noise in the CCD (left), and in the CMOS (right) [69]

The fixed pattern noise is defined by considering the linear model for the sensor in the form of a relation (5). In this definition, the intensity of the output pixel is give by the value  $y$  and the function of the received light is  $s$ .

$$(2) \quad y = Gs + y_{offset}$$

In the above operation, the parameters  $G$  and  $y_{offset}$  are respectively, the gain and the intensity offsets per pixel. Ideally, these values are equal to 1 and zero. If we want to express the above equation for every pixel of an array  $M * N$ , then we have:

$$(3) \quad y(m, n) = G(m, n)s(m, n) + y_{offset}(m, n)$$

## 4.6.2 Image pre-processing

An important part of an image processing system or a system that processes activities based on visual information, is the pre-processing before the proposed method is performed. Image pre-processing is strongly dependent on the problem location and the image data to be analysed. For example, special pre-processing objectives can include reducing the influence of noise, elimination of artefacts and interferences, improving the image contrast, scaling the grey scale range, or normalizing the image size.

It is necessary to carry out these processes on the images before the implementation of the original or proposed method in order to achieve the best results in relation to the aims of the research or the project, as well as the definition of the problem. With image pre-processing methods, the quality of the medical image and its information content, can be substantially increased with regard to subsequent processing processes and the representation of specific image structures. [[Heinz Handels, Medizinische Bildverarbeitung].]

Digital data can be processed and analysed with the computer. This process is implemented to enhance and improve the quality of the data and the visual interpretations. Special themes or information can also be retrieved from the image. The computer performs all these processes automatically.

Each image consists of many small squares (pixels). Every pixel has a digital number that indicates the brightness of that pixel. These pictures are the so-called digital images. Digital images have rows and columns [70].

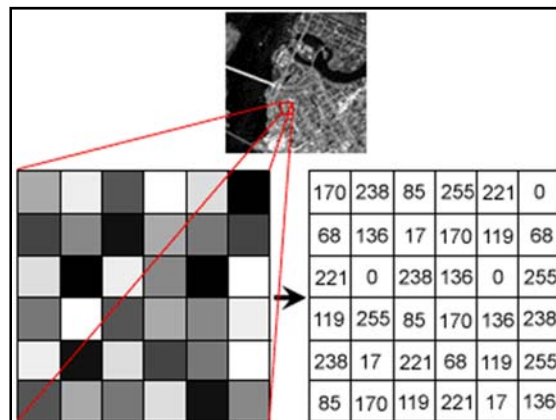
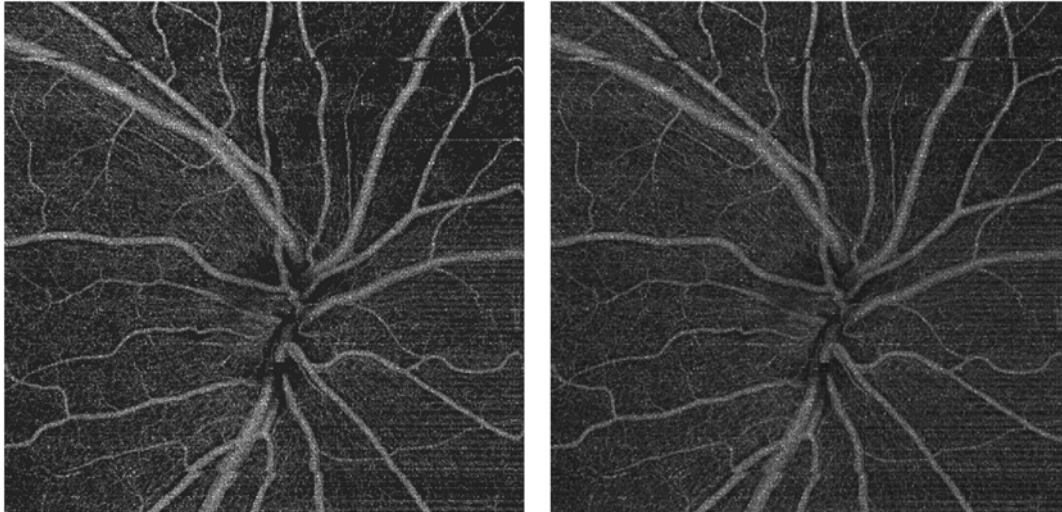


Figure 21: Pixel representation

### Image precision:

The image precision depends on the number of pixels. In the following Figure 22. Figure 22: Difference of precision (Left 4Bit, Right 16Bit)





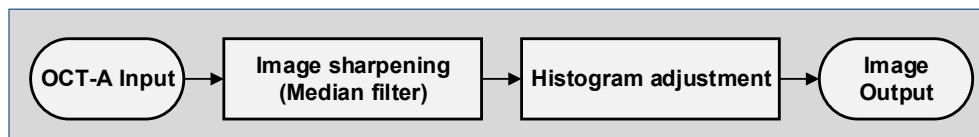
**Figure 22: Difference of precision (Left 4Bit, Right 16Bit)**

An image can be represented by a two-dimensional function:  $f(x,y)$ . Where  $X$  and  $Y$  are spatial coordinates and the value of  $f$  at each point is the intensity of the image at that point. The term grayscale is also referred to as a monochrome image. Colour images consist of many two-dimensional images. When the  $X$  and  $Y$  values and a value of  $f(x, y)$  are discrete and limited expressions, the image will be called a digital image. The digitization of the values of  $X$  and  $Y$  is called sampling and digitizing the value of  $f(x, y)$  is quantization.

Application methods for pre-processing:

- Image sharpening
- Histogram adjustment

The general algorithm in the flowchart (6) shown below, represents the entire process of pre-processing on the image.



**Flowchart 6: Pre-processing steps**

### 4.6.3 Image de-noising with median filter

A median filter is a non-linear filter mainly used to remove impulsive noise from images [71].

The images we have for the processing process are often accompanied by unwanted signals that are called noise, and which destroy the image information. Although the undesired signals do not greatly affect the image, the removal of these interfering signals is essential and necessary. Interfering signals in images cause problems in pictures such as medical images,

aerial images and satellite-transmitted images. There are different types of noise, the most important are:

- Salient noise
- White line dropout noise
- Shadowing noise
- Salt & pepper noise

Some of these noises can greatly affect the process of the image processing, especially in edge detection, segmentation, data compression and object detection [72]. However, the median filter which uses masking, begins to scroll through all the pixels. This 3x3 filter works based on scrolling and uses the adjacent pixels. A schematic of this filter is shown in Figure 23 [73].

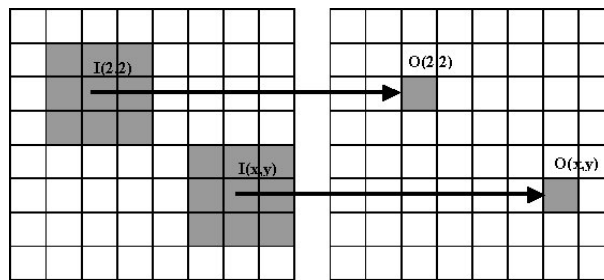


**Figure 23: 3x3 spatial filtering**

The low-pass filter uses the median of a neighbour ( $m * n$ ). Their method is to arrange all neighbour's pixels in ascending order to select the middle element of the ordered numbers, and replace the value of central pixel with this value. The reason for using the low-pass filter is that in the process of imaging from the moment of imaging to the moment of displaying the final image, the electrical and environmental factors will occur difference noise frequencies depending on the nature of the noise. Thus, the noise and the disturbance factor are not reflected at low frequencies, but at high frequencies on the image.

It should be noted that the low-pass filter can be more useful for the removal of salt and pepper noise. An example of how this filter works is shown in Figure 24.

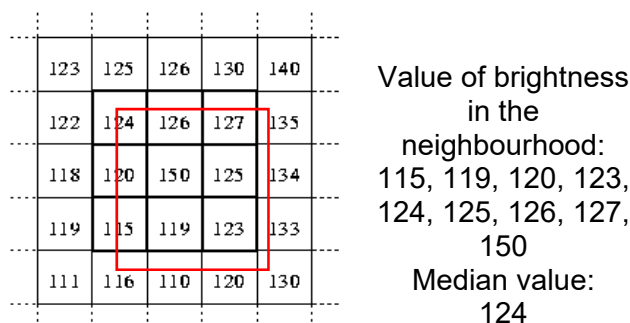


**Figure 24: An example of Median-filter [74]**



However, when beginning to process edge pixels, since some of the pixels of the mask correspond to the image to the outside, we will encounter a black border after masking. To stop this happening, it is possible to copy the border of the original image, place it next to the previous frame, and then start to scroll or set the edge values to zero, and then begin processing. In the image shown in Figure 26 is a noisy image, a filter programmed with Matlab will be applied to this image. Figure 25 shows the image after noise reduction with Median filter.

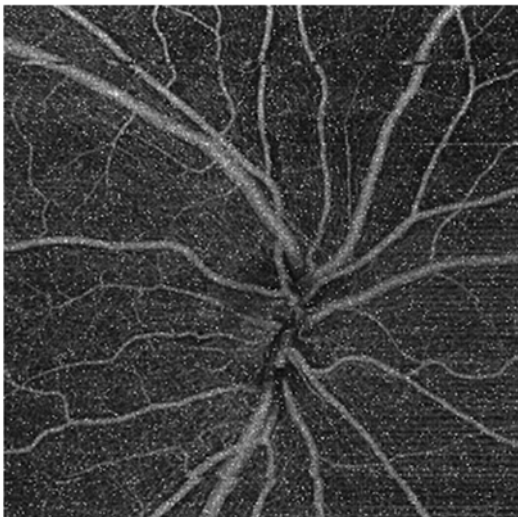


**Figure 26: Image with salt & pepper noise by 0.006 noise density**

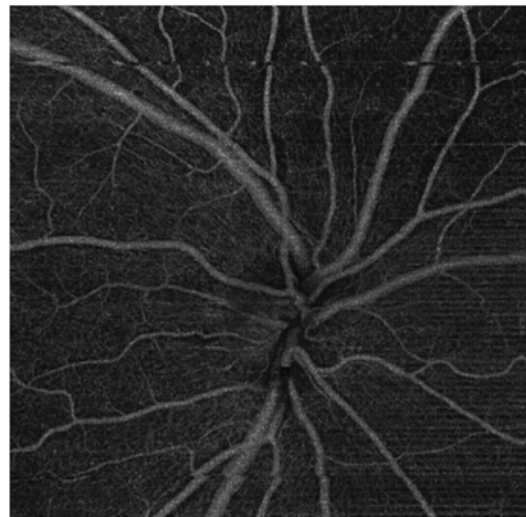


**Figure 25: Image denoised by Median filter**

#### **4.6.4 Histogram equalization**

Changing the histogram is one of the simplest and most useful techniques in image processing. In fact, this technique is commonly used to improve the contrast quality of an image. It can be predicated that it is a general way to increase the contrast of an image [75]. The histogram is a graph, which shows the frequencies of the grey values of an image, ordered by brightness. Assuming that the input image is a grey scale image with 256 brightness levels, then each image pixel can have a value in the interval of [255...0]. To obtain a histogram of an image, it will be sufficient to scroll all the image pixels to calculate the number of pixels for each brightness level

The histogram of the image after noise reduction with Median filter is displayed in Figure 27.

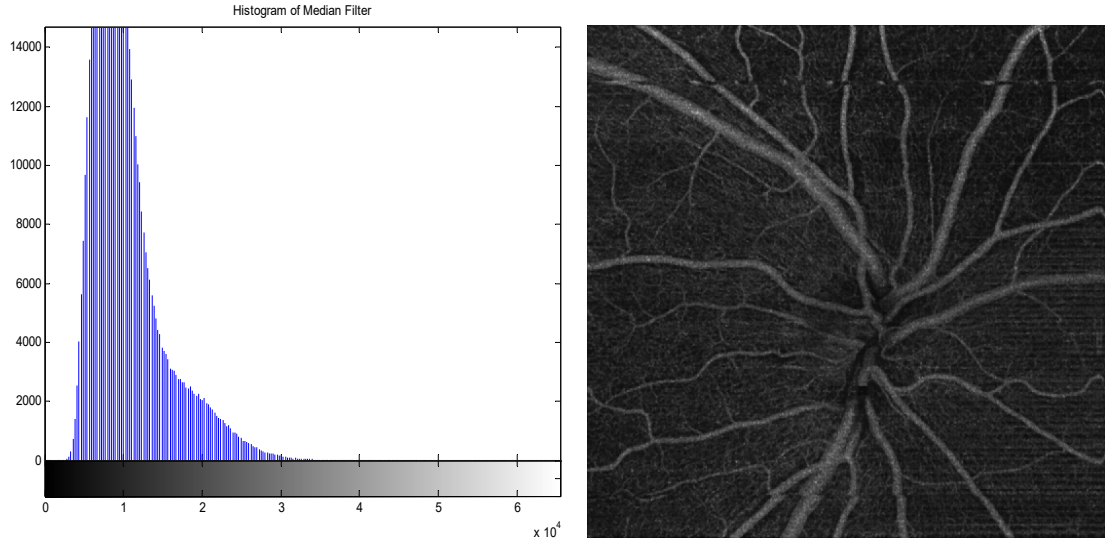


**Figure 27: Histogram of image after de-noising**

The normal histogram is also calculated by dividing the histogram values into the total number of image pixels. The histogram normalization causes the histogram values to be in the range [0.1]. But adjusting the histogram has the effect of increasing the contrast of those pixels of the image which have a lower contrast value. If an image has a low contrast, this means that the difference between the smallest and the brightest pixels of the image is small. Through adjusting the histogram, the contrast of the input image will be increased as much as possible. The following algorithm shows the method of adjusting a histogram. The program for the histogram calculation and its adjustment is achieved by programming in Matlab.

In fact, for the image  $X$ , if the grayscale is in the range  $[X_0, X_{L-1}]$ , the probability density function in equation (1) is equal to:

$$(4) p(X_k) = \frac{n_k}{n}$$

In this equation,  $n_k$  is the frequency of the repetition of the brightness level  $X_k$ , and the  $X_k$  is the value for the light intensity  $k$ . We also know that  $k$  belongs to the interval  $k = 0, 1, \dots, L - 1$ , the cumulative distribution function (CDF) is defined in the form of equation (2):

$$(5) c(x) = \sum_{j=0}^k p(X_j)$$

Here for  $c(X_{L-1}) = 1$  and the function  $f(x)$  the cumulative distribution function (CDF) is shown in equation (3):

$$(6) f(x) = X_0 + (X_{L-1} - X_0) * c(x)$$

The output image is called after the adjustment of the histogram  $Y$ , in which it is defined:  $Y = \{Y_k\}$  and also  $Y = f(X)$ . Thus, in equation (4),  $Y$  is equal to:

$$(7) \{f(X_k), \forall X_k \in X\}$$

The main idea is to extend the mapping of grayscale based on the probability distribution of the grey input levels [75]. Note that information about the edges of the image must be retained during the histogram equalization. In Figure 28, the adjustment of the histogram has been performed after the noise reduction.

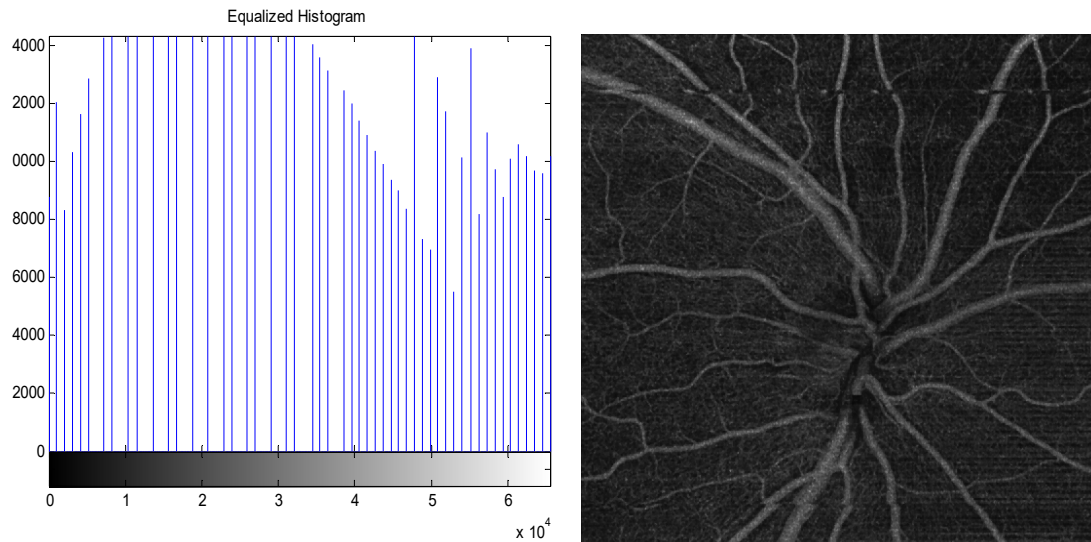
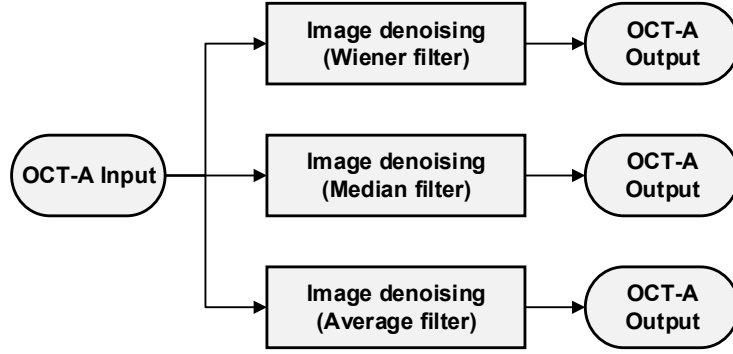


**Figure 28: OCTA en-face Image and after Histogram equalization**

#### 4.6.5 Review of used noise removal techniques

Before designing a new algorithm to eliminate fixed pattern noise, we first examined the filters and algorithms that have been introduced to improve images and remove noise so far, and applied them to images of stars.

The general steps for finding the best method to reduce the noises are as follows:



**Flowchart 7: Steps to find the best method for De-noising**

The first method was to use a Wiener filter, which is an adaptive filter commonly used to improve images, especially spatial images. We then examined the performance of middle and median filters, which are commonly used in image processing to remove extreme changes from pixels. In this section, we first give a brief description of the mechanism of the described filters, and then describe an algorithm for removing fixed pattern noise from images. Finally, after comparing the methods using MATLAB software, we choose the algorithm with the highest reduction of variance in the average response of the pixels in the adjacent rows. All the algorithms are first applied to the Figure 32, and after selecting the appropriate algorithm, we applied the selected method to a series of images taken by the SS-OCT. It is worth mentioning, that in all steps, for the sake of clarity, we define the result of the algorithm in the form of the difference between the original image and the modified image.

#### 4.6.5.1 Wiener filter

The Wiener filter is a low-pass filter, which calculates the output pixel value in a comparative method based on the statistical properties of the neighbouring pixels, such as mean and standard deviation.

$$(8) \quad \mu = \frac{1}{NM} \sum_{n_1, n_2 \in \eta} \alpha(n_1, n_2)$$

$$(9) \quad \sigma^2 = \frac{1}{NM} \sum_{n_1, n_2 \in \eta} \alpha^2(n_1, n_2) - \mu^2$$

In the above relations,  $\eta$  is a neighbourhood of  $N \times M$  around each pixel. In this case, the pixel value is changed as follows.

$$(10) \quad b(n_1, n_2) = \mu + \frac{\sigma^2 - v^2}{\sigma^2} (\alpha(n_1, n_2) - \mu)$$

In (9), the  $v^2$  is the variance of the noise in the image. If  $v^2$  is unknown, the mean of estimated local deviations is used. We can show the Wiener filter function by assuming a  $5 \times 5$  neighbourhood on the Figure 29 as shown below.

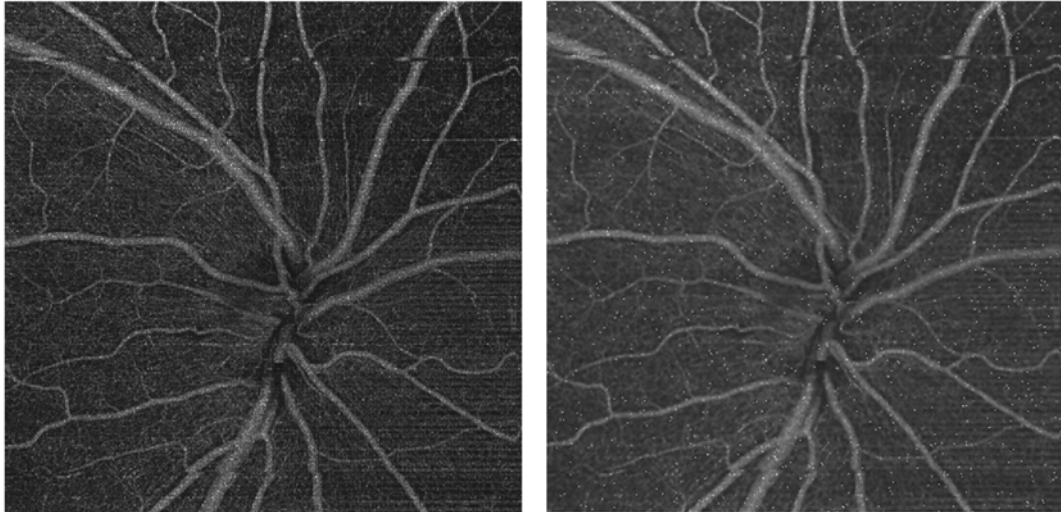


**Figure 29: Original image (left), image de-noised by Wiener filter (right)**

As has been previously said, the difference between the original and the corrected image is equal to the noise in the image, and should be the same as the lines appearing in Figure 32, depending on the fixed pattern noise. However, as shown in Figure 29, Wiener's filter failed to eliminate these lines perfectly.

#### **4.6.5.2 Average and Median filter**

As well as other filters used to process images, the average and median filters are used to reduce the difference between adjacent pixel values. In both filters, the average and median of a window are embedded in the centre of each pixel. (Usually a 3 by 3 window), i.e. for each pixel there are eight neighbours. The window is intended to be navigated to all areas of the image matrix. In fact, each pixel should be placed once in the centre of the window and the corrected value of that area decided based on the values of its neighbouring pixels. In the median filter, the average value of the neighbouring pixels of each pixel is considered as the new pixel value. In Figure 30, you see the result of applying the median filter.

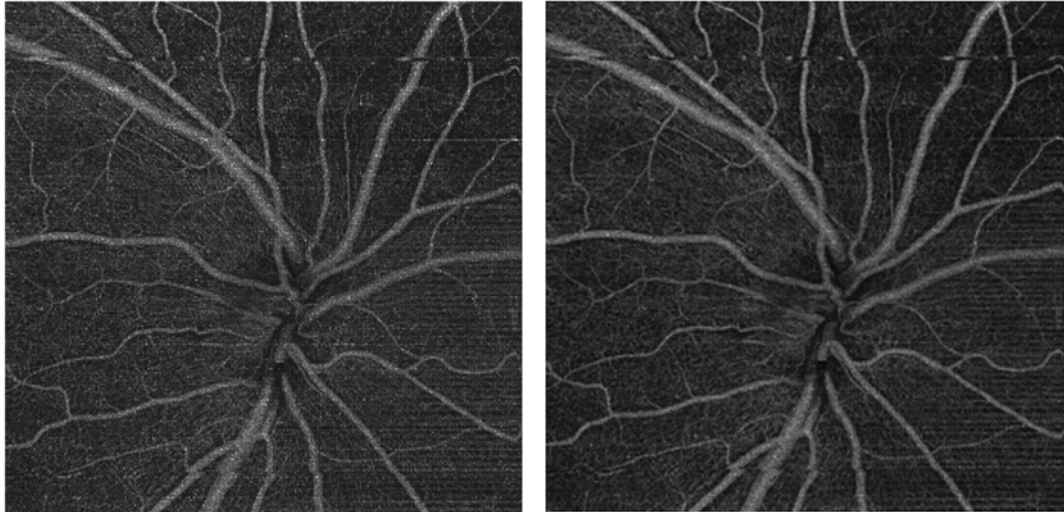


**Figure 30: Original image (left), image de-noised by median filter (right)**

As can be seen from the above result, the median filter failed to eliminate the fixed pattern noise and the result is far worse than that of the Wiener filter. In the average filter, the average pixel values of each pixel are averaged and the result is considered as the new pixel value. Figure 31 shows the result of applying the average filter on Figure 32. As you can see in Figure 31, this filter could not eliminate the static pattern noise, and in addition to the undesirable noise removal result, the processing time is longer than that of the previous two filters.

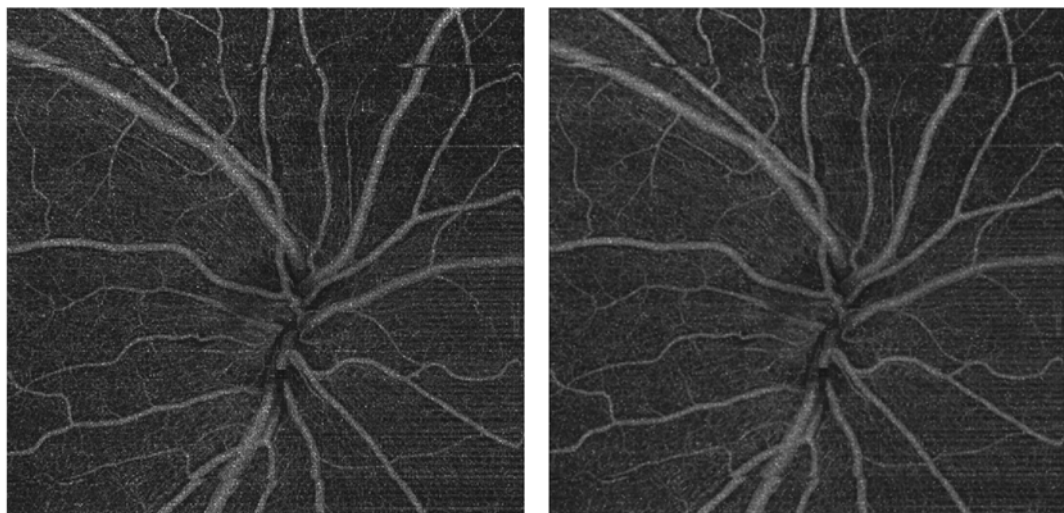


**Figure 31: Original image (left), image de-noised by average filter (right)**

In fact, the effect of using these three types of Wiener, median and average filter is to somehow normalize the image due to the staining of the original, fixed pattern noise. These three types of filters are in fact somehow normalizing the noise in the image if the original image before using the three types of filters, is as in Figure 32.

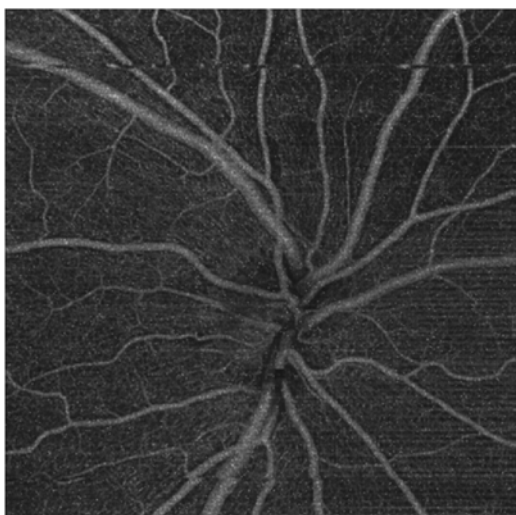


**Figure 32: Original OCTA en-face image**

In this case, if we subtract the original image and noisy image and multiply it 50 times, the noise level in the image will be well defined, which is clearly shown in the Figure 33 below. Of course, the magnification of this noise is needed to better detect this noise, or if the noise level is much smaller than that specified in the image.

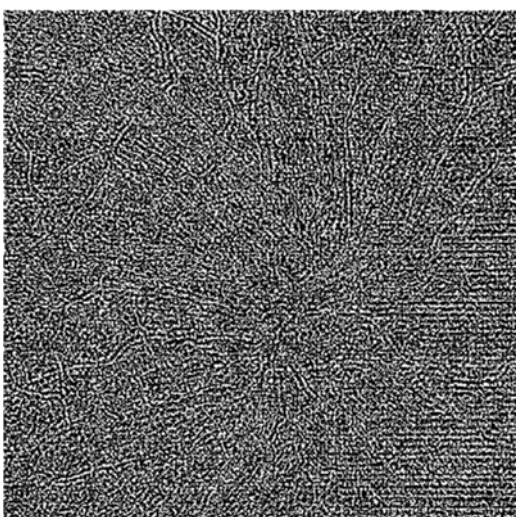
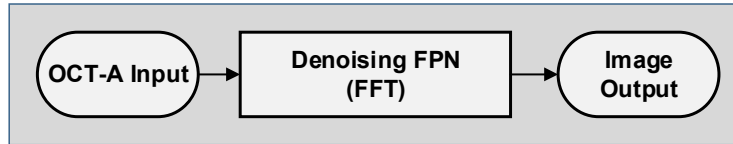


**Figure 33: 50 times noise**

In the following section, we will examine the proposed method for eliminating the stripe artefacts in OCT-A images due to motion artefacts. As mentioned before, they can be treated as fixed pattern noise (FPN) in the image.



Flowchart 8: Steps to reduce the FPN

#### 4.6.5.3 Fast Fourier Transform

Fast Fourier Transform (FFT) is the name of the algorithm for the fast and efficient execution of direct and inverse Fourier transforms. There are many fast differential Fourier transform algorithms which cover a huge range of mathematics: from simple calculations of complex numbers to number theory. A fast Fourier transform decomposes a string of values into components with different frequencies. The calculation of a discrete Fourier transform for  $n$  points, requires the use of the definition  $O(n^2)$  of math operations, while the fast Fourier transform can calculate the same results in  $O(n \log n)$  operations. This difference in speed can be very impressive, especially for a large data set. When  $n$  may be thousands or millions of operations, the calculation time in some cases can be reduced by several times, and its improvement is approximately  $N/\log_2^n$  [76].

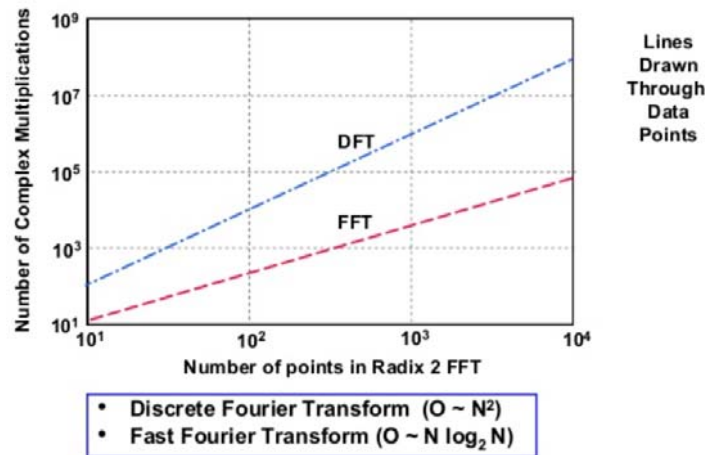


Figure 34: DFT vs. FFT

The Fourier transform is a fundamental method in signal processing. By this method, signals from the representation {time, sample value} can be converted into the representation {frequency fraction, amplitude, phase}. Many operations, e.g. filters, can be implemented more easily in the frequency range. The signal is then transformed back again with the inverse Fourier transform.

$$F(u) = \frac{1}{M} \sum_{x=0}^{M-1} f(x) e^{-\frac{j2\pi ux}{M}}, u = 0, 1, 2, \dots, M-1$$



To apply a Fourier filter to the image for stripe noise elimination, we used the fast Fourier transform filter. For this, see the original image, Figure 35. This image is full of stripe noises. The noise in these OCTA images is a fixed pattern noise that is represented in the images as horizontal lines, which means that these lines or noise are still present in the image after applying the Wiener, median and average filters. The image is only equalized.

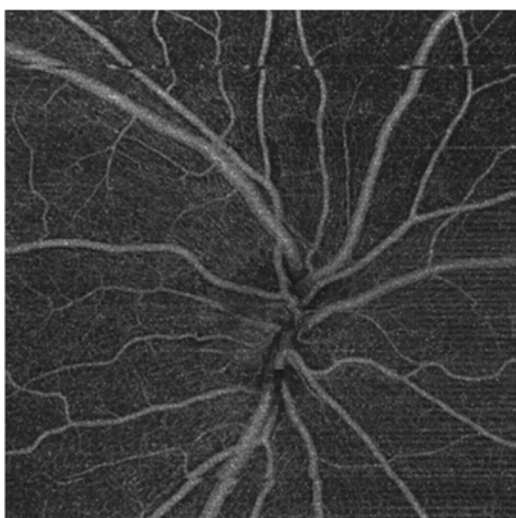


**Figure 35: Original OCTA en-face image with noise**

The result after applying a fast discrete Fourier transform (DFT) is shown in Figure 36, above.

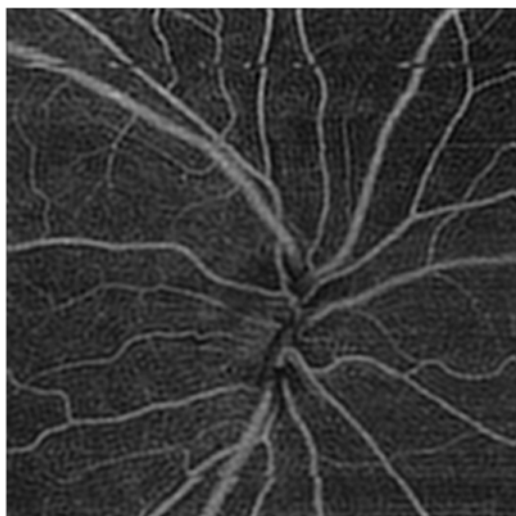


**Figure 36: OCTA en-face after De-noising with FFT**

To better illustrate the effect of this filter, we used Figure 37, in this figure it is clear that the noise has been removed well.

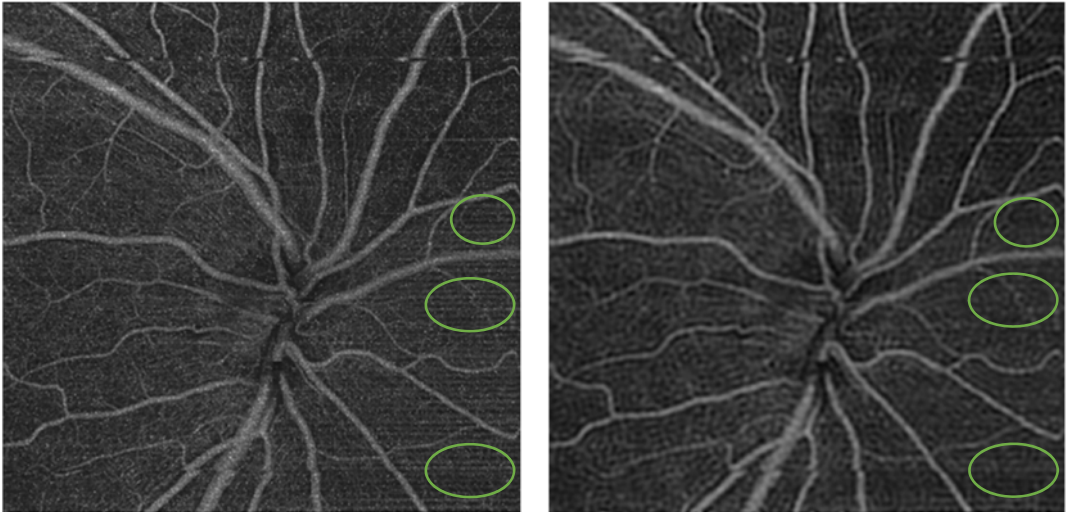


Figure 37: Original OCTA en-face image with noise (left), image after De-noising with FFT

The behaviour of this filter was examined several times in a frequency range between 55 and 65 Hz. Through trial and error method, the answers were examined in this area. This method has been shown that the results of used frequencies above or below 62Hz were certainly not satisfactory. The filter implemented for this image has a cut-off spatial frequency of  $f_c = 62 \text{ Hz}$  that is determined by trial and error, as shown in Figure 38.

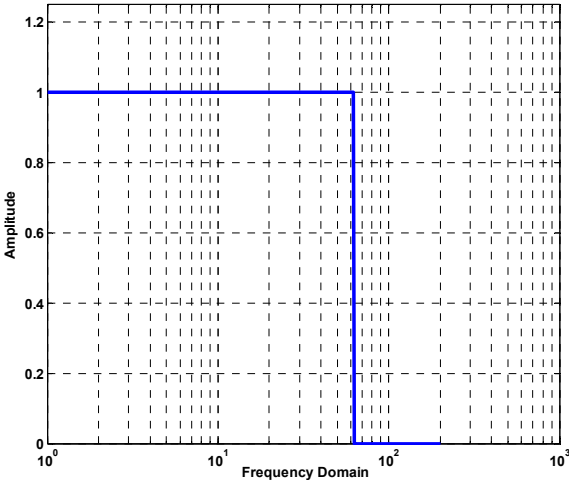


Figure 38: A demonstration of low frequency pass filter response to de-noising



## 5 Results and Conclusions

The goal, which was achieved, was to implement a method that automatically extracts various layers of the retina in OCT-tomography images by using graph based medical image processing methods. In the chapter on image processing, important information has been provided for understanding the image processing techniques that are used to segment the images, which are introduced later. In this chapter, a general definition of the image was given. The chapter also deals with the pre-processing of OCT tomography images. For this work, an in-depth knowledge of OCT images and their digital image processing was required. The techniques used for the segmentation and detection of layers in the OCT tomogram images were also explained in this chapter, because they allow different layers of the retina to be extracted in an automated manner. A definition of noise, particularly about the FPN in OCT angiography images, has been provided, and the various methods for removing this noise have been explained. The de-noising later turned out to be a very important part of this work. Therefore, it was necessary to mention the procedures that can be used for de-noising.

It was found that the proposed method [65], which was implemented for segmentation and tested on a series of OCT B-scan images, is computationally time consuming. Dijkstra's algorithm is used in this method to discover the shortest paths in the graphs. Based on the dataset which we had and have tested, and the CPU used, the run-time of segmentation-algorithm of individual images is different. We expect that this could be accelerated by employing GPU programming.

We then tried to eliminate the noise in OCT angiography images. After several attempts, it was found that stripe artifacts, which are visible in OCTA images, can be treated as fixed pattern noise, which makes the extraction of angiographic features difficult. To reduce this noise and eliminate it, we used FFT filtering. The noise is successfully reduced. But, the problem with this method was that some very fine details in images along the direction of the stripe artefacts e.g. very thin vessels, also became less visible and recognizable.

In the process of this work, it became clear that the quality of the image processing results depended on the medical image processing method, but also on the imaging system, techniques and the stability of the target objects. It was also found that the methods and algorithms can have different effects on different data.

The developed tools will nevertheless be important for precise evaluation of distinct vascular beds within the retina, which in the future should allow for a better and early diagnosis of retinal diseases.



# Acronyms

- ADC: Analog Digital Converter
- AMD: Age Dependent Macular Degeneration
- CCD: Charge Coupled Device
- CDF: Cumulative Distribution Function
- CMOS: Complementary Metal Oxide Semiconductor
- CNV: Choroidal Neovascularization
- CPU: Central Processing Unit
- DFT: Discrete Fourier Transform
- EDI-OCT: Enhanced Depth Imaging-OCT
- FD-OCT: Frequency Domain OCT
- FFT: Fast Fourier Transform
- FOV: Field Of View
- FPN: Fixed-Pattern Noise
- FT: Fourier Transform
- GCL: Ganglion Cell Layer
- GMM: Gaussian Mixed Model
- GPU: Graphics Processing Unit
- ILM: Inner Limiting Membrane
- INL: Inner Nuclear Layer
- IPL: Inner Plexiform Layer
- IS: Inner Segment
- MRI: Magnetic Resonance Imaging
- MS: Multiple Sclerosis
- NFL: Nerve Fiber Layer
- OCT: Optical Coherence Tomography
- OCTA: Optical Coherence Tomography Angiography
- OLM: Outer Limiting Membrane
- ONL: Outer Nuclear Layer

- OPL: Outer Plexiform Layer
- OS: Outer Segment
- RGC: Retinal Ganglion Cells
- RPE: Retinal Pigment Epithelium
- SD-OCT: Spectral Domain-OCT
- SS-OCT: Swept-Source-OCT
- TD-OCT: Time Domain OCT

## List of figures

Figure 1: Human Eye Structure [5].....	5
Figure 2: Different layers of retina .....	7
Figure 3: Parts of Optic Nerve [26].....	9
Figure 4: Healthy Optic Nerve and with Glaucoma [31] .....	10
Figure 5: Normal Vision and with Glaucoma [33] .....	11
Figure 6: Tissue optical window (Water, Hb) [36].....	13
Figure 7: Michelson’s Interferometry.....	14
Figure 8: Resolution depth of the penetration .....	15
Figure 9: TD-OCT and SD-OCT .....	16
Figure 10: Target retinal layers of a cross-sectional SDOCT image (B-scan) centered at the macula [65].....	25
Figure 11: Example graph weights (adjacency matrix) [65] .....	26
Figure 12: Automatic endpoint initialization.....	27
Figure 13: A graph example for Dijkstra’s algorithm .....	28
Figure 14: Input Image .....	29
Figure 15: RPE Boundary .....	30
Figure 16: NFL boundaries.....	31
Figure 17: RPE OS boundaries.....	32
Figure 18: ONL-IS boundary .....	33
Figure 19: Segmented image .....	34
Figure 20: Effect of fixed pattern noise in the CCD (left), and in the CMOS (right) [69].....	35
Figure 21: Pixel representation .....	36
Figure 22: Difference of precision (Left 4Bit, Right 16Bit) .....	37
Figure 23: 3x3 spatial filtering .....	38
Figure 24: An example of Median-filter [74] .....	38
Figure 25: Image denoised by Median filter .....	39
Figure 26: Image with salt & peppr noise by 0.006 noise density .....	39
Figure 27: Histogram of image after de-noising .....	40
Figure 28: OCTA en-face Image and after Histogram equalization .....	41
Figure 29: Original image (left), image de-noised by Wiener filter (right).....	43
Figure 30: Original image (left), image de-noised by median filter (right) .....	44
Figure 31: Original image (left), image de-noised by average filter (right) .....	44
Figure 32: Original OCTA en-face image .....	45
Figure 33: 50 times noise .....	45
Figure 34: DFT vs. FFT .....	46
Figure 35: Original OCTA en-face image with noise .....	47
Figure 36: OCTA en-face after De-noising with FFT .....	47
Figure 37: Original OCTA en-face image with noise (left), image after De-noising with FFT .....	48
Figure 38: A demonstration of low frequency pass filter response to de-noising .....	48



## List of flowcharts

Flowchart 1: General methodology .....	22
Flowchart 2: Stages of the medical image processing [62] .....	23
Flowchart 3: Segmentation general steps .....	24
Flowchart 4: Segmentation algorithm .....	25
Flowchart 5: Detailed segmentation algorithm .....	29
Flowchart 6: Pre-processing steps .....	37
Flowchart 7: Steps to find the best method for De-noising.....	42
Flowchart 8: Steps to reduce the FPN .....	46

# Bibliography

- [1] Kingman, S. (2004). Glaucoma is second leading cause of blindness globally. *Bulletin of the World Health Organization*, 82(11), 887-888.
- [2] Casson, R. J., Chidlow, G., Wood, J. P., Crowston, J. G., & Goldberg, I. (2012). Definition of glaucoma: clinical and experimental concepts. *Clinical & experimental ophthalmology*, 40(4), 341-349.
- [3] R. Krammer, *Medizintechnik*.
- [4] Spaide, R. F., Fujimoto, J. G., & Waheed, N. K. (2015). Image artifacts in optical coherence tomography angiography. *Retina (Philadelphia, Pa.)*, 35(11), 2163-2180.
- [5] "eyerisvision," [Online]. Available: <http://www.eyerisvision.com/anatomy-of-the-eye.html>. [Accessed 21 09 2017].
- [6] Litzinger, T. C., & Rio-Tsonis, K. D. (2002). *Eye anatomy*. eLS.
- [7] Kaufman, P. L., Adler, F. H., Levin, L. A., & Alm, A. (2011). *Adler's physiology of the eye: Ocular circulation*. Elsevier Health Sciences.
- [8] Chung, S. E., Kang, S. W., Lee, J. H., & Kim, Y. T. (2011). Choroidal thickness in polypoidal choroidal vasculopathy and exudative age-related macular degeneration. *Ophthalmology*, 118(5), 840-845.
- [9] J. P, O. S, T. A, Y. K, H. M, H. M and e. al., "Assessment of macular choroidal thickness by optical coherence tomography and angiographic changes in central serous chorioretinopathy," *Ophthalmology*, pp. 119 (8): 1666-78, 2012.
- [10] Brown, J. S., Flitcroft, D. I., Ying, G. S., Francis, E. L., Schmid, G. F., Quinn, G. E., & Stone, R. A. (2009). In vivo human choroidal thickness measurements: evidence for diurnal fluctuations. *Investigative ophthalmology & visual science*, 50(1), 5-12.
- [11] Coleman, D. J., Silverman, R. H., Chabi, A., Rondeau, M. J., Shung, K. K., Cannata, J., & Lincoff, H. (2004). High-resolution ultrasonic imaging of the posterior segment. *Ophthalmology*, 111(7), 1344-1351.
- [12] Sarks, S. H. (1976). Ageing and degeneration in the macular region: a clinico-pathological study. *British Journal of Ophthalmology*, 60(5), 324-341.
- [13] Spaide, R. F., Koizumi, H., & Pozzoni, M. C. (2008). Enhanced depth imaging spectral-domain optical coherence tomography. *American journal of ophthalmology*, 146(4), 496-500.
- [14] Považay, B., Hermann, B., Unterhuber, A., Hofer, B., Sattmann, H., Zeiler, F., Morgan, J., Falkner-Radler, C., Glittenberg, C., Blinder, S. and Drexler, W. (2007). , "Three-dimensional optical coherence tomography at 1050 nm versus 800 nm in retinal

pathologies: enhanced performance and choroidal penetration in cataract patients. *Journal of Biomedical Optics*, 12(4), p.041211”.

- [15] Margolis, R., & Spaide, R. F. (2009). A pilot study of enhanced depth imaging optical coherence tomography of the choroid in normal eyes. *American journal of ophthalmology*, 147(5), 811-815.
- [16] Kajić, V., Esmaeelpour, M., Považay, B., Marshall, D., Rosin, P. L., & Drexler, W. (2012). Automated choroidal segmentation of 1060 nm OCT in healthy and pathologic eyes using a statistical model. *Biomedical optics express*, 3(1), 86-103.
- [17] B. Shaberman, “Blindness.org,” [Online]. Available: <http://www.blindness.org/blog/index.php/fascinating-facts-about-retinal-cells/>. [Accessed 21 09 2017].
- [18] Chen, J., Cranton, W., & Fihn, M. (Eds.). (2012). *Handbook of visual display technology* (Vol. 131). Berlin: Springer.
- [19] Masland, R. H. (2001). The fundamental plan of the retina. *Nature neuroscience*, 4(9), 877-886.
- [20] Huang, D., Swanson, E. A., Lin, C. P., Schuman, J. S., Stinson, W. G., Chang, W., ... & Fujimoto, J. G. (1991). Optical coherence tomography. *Science (New York, NY)*, 254(5035), 1178.
- [21] Asrani, S., Rosdahl, J. A., & Allingham, R. R. (2011). Novel software strategy for glaucoma diagnosis: asymmetry analysis of retinal thickness. *Archives of ophthalmology*, 129(9), 1205-1211.
- [22] H. Qi and J. F. Head, “Asymmetry analysis using automatic segmentation and classification for breast cancer detection in thermograms,” *In Engineering in Medicine and Biology Society*, 2001.
- [23] Park, J. J., Oh, D. R., Hong, S. P., & Lee, K. W. (2005). Asymmetry analysis of the retinal nerve fiber layer thickness in normal eyes using optical coherence tomography. *Korean Journal of Ophthalmology*, 19(4), 281-287.
- [24] Budenz, D. L. (2008). Symmetry between the right and left eyes of the normal retinal nerve fiber layer measured with optical coherence tomography (an AOS thesis). *Transactions of the American Ophthalmological Society*, 106, 252.
- [25] Bergua, A. (2017). *Das menschliche Auge in Zahlen*.
- [26] “Slideshare Anatomy-of-optic-nerve-and-its-blood-supply,” [Online]. Available: <https://www.slideshare.net/vijayjoshi311/anatomy-of-optic-nerve-and-its-blood-supply>. [Accessed 26 09 2017].
- [27] Hayreh, S. S., & Jonas, J. B. (2001). Optic disc morphology after arteritic anterior ischemic optic neuropathy. *Ophthalmology*, 108(9), 1586-1594.
- [28] Allingham, R. R., Damji, K. F., Freedman, S. F., Moroi, S. E., Rhee, D. J., & Shields, M. B. (2012). *Shields textbook of glaucoma*. Lippincott Williams & Wilkins.

- [29] Barton, K., & Hitchings, R. A. (2013). Introduction. In *Medical Management of Glaucoma* (pp. 1-32). Springer Healthcare Ltd..
- [30] Flammer, J., Orgül, S., Costa, V. P., Orzalesi, N., Krieglstein, G. K., Serra, L. M., ... & Stefánsson, E. (2002). The impact of ocular blood flow in glaucoma. *Progress in retinal and eye research*, 21(4), 359-393.
- [31] "Glaucoma," [Online]. Available: <http://www.glaucoma.org/glaucoma/optic-nerve-cupping.php>. [Accessed 26 09 2017].
- [32] "Uni. Klinik Augenklinik, Uni Essen," [Online]. Available: <https://www.uni-due.de/augenklinik/glaukom.shtml>. [Accessed 29 07 2017].
- [33] "Eyerisvision," [Online]. Available: <http://www.eyerisvision.com/glaucoma.html>. [Accessed 21 09 2017].
- [34] Newell, F. (1982). *Ophthalmology, principles and concepts*. St. Louis: Mosby.
- [35] Gupta, D. (2005). *Glaucoma diagnosis and management*. Lippincott Williams & Wilkins.
- [36] Benov, L. (2015). Photodynamic therapy: current status and future directions. *Medical Principles and Practice*, 24(Suppl. 1), 14-28.
- [37] Drexler, W., Morgner, U., Ghanta, R. K., Kärtner, F. X., Schuman, J. S., & Fujimoto, J. G. (2001). Ultrahigh-resolution ophthalmic optical coherence tomography. *Nature medicine*, 7(4), 502.
- [38] Schneeberg, A. E., & Göbel, W. (2003). Diagnostik und Verlaufskontrolle des nichtdiabetischen Makulaödems mithilfe der optischen Kohärenztomographie (OCT). *Der Ophthalmologe*, 100(11), 960-966.
- [39] Drexler, W., Morgner, U., Ghanta, R. K., Kärtner, F. X., Schuman, J. S., & Fujimoto, J. G. (2001). Ultrahigh-resolution ophthalmic optical coherence tomography. *Nature medicine*, 7(4), 502.
- [40] "Biophotonics uni-hannover," [Online]. Available: <https://www.biophotonics.uni-hannover.de/498>. [Accessed 28 06 2017].
- [41] "Biophotonics uni-hannover," [Online]. Available: <https://www.biophotonics.uni-hannover.de/498.html>. [Accessed 28 06 2017].
- [42] Heimann, H., Kellner, U., & Foerster, M. H. (2006). *Angiographie-Atlas des Augenhintergrundes*. Georg Thieme Verlag.
- [43] Hillmann, D., Bonin, T., Lührs, C., Franke, G., Hagen-Eggert, M., Koch, P., & Hüttmann, G. (2012). Common approach for compensation of axial motion artifacts in swept-source OCT and dispersion in Fourier-domain OCT. *Optics express*, 20(6), 6761-6776.
- [44] Fang, P. P., Lindner, M., Steinberg, J. S., Müller, P. L., Gliem, M., Issa, P. C., ... & Holz, F. G. (2016). Klinische Anwendungen der OCT-Angiographie. *Der Ophthalmologe*, 113(1), 14-22.

- [45] Zhang, M., Wang, J., Pechauer, A. D., Hwang, T. S., Gao, S. S., Liu, L., ... & Jia, Y. (2015). Advanced image processing for optical coherence tomographic angiography of macular diseases. *Biomedical optics express*, 6(12), 4661-4675.
- [46] Izatt, J. A., Choma, M. A., & Dhalla, A. H. (2015). Theory of optical coherence tomography. *Optical Coherence Tomography: Technology and Applications*, 65-94.
- [47] Al-Mujaini, A., Wali, U. K., & Azeem, S. (2013). Optical coherence tomography: clinical applications in medical practice. *Oman medical journal*, 28(2), 86.
- [48] Fang, P. P., Lindner, M., Steinberg, J. S., Müller, P. L., Gliem, M., Issa, P. C., ... & Holz, F. G. (2016). Klinische Anwendungen der OCT-Angiographie. *Der Ophthalmologe*, 113(1), 14-22.
- [49] Huang, S., Shen, M., Zhu, D., Chen, Q., Shi, C., Chen, Z., & Lu, F. (2016). In vivo imaging of retinal hemodynamics with OCT angiography and Doppler OCT. *Biomedical optics express*, 7(2), 663-676.
- [50] M. Peter, C. Gyger and P. W. Hasler, "A pilot study to image the vascular network of small melanocytic choroidal tumors with speckle noise-free 1050-nm swept source optical coherence tomography (OCT choroidal angiography)," *Graefe's Archive for Clinical and Experimental Ophthalmology* 254.6, p. 1201, 2016.
- [51] Liu, L., Gao, S. S., Bailey, S. T., Huang, D., Li, D., & Jia, Y. (2015). Automated choroidal neovascularization detection algorithm for optical coherence tomography angiography. *Biomedical optics express*, 6(9), 3564-3576.
- [52] Varga, B. E., Gao, W., Laurik, K. L., Tátrai, E., Simó, M., Somfai, G. M., & DeBuc, D. C. (2015). Investigating tissue optical properties and texture descriptors of the retina in patients with multiple sclerosis. *PLoS one*, 10(11), e0143711.
- [53] Tang, F. Y., Ng, D. S., Lam, A., Luk, F., Wong, R., Chan, C., ... & Lai, F. (2017). Determinants of Quantitative Optical Coherence Tomography Angiography Metrics in Patients with Diabetes. *Scientific Reports*, 7, "Determinants of Quantitative Optical Coherence Tomography Angiography Metrics in Patients with Diabetes".
- [54] Munk, M. R., Giannakaki-Zimmermann, H., Berger, L., Huf, W., Ebnetter, A., Wolf, S., & Zinkernagel, M. S. (2017). OCT-angiography: A qualitative and quantitative comparison of 4 OCT-A devices. *PLoS one*, 12(5), e0177059.
- [55] Huang, D., Jia, Y. and Liu, L., Oregon Health & Science University, 2016. Systems and methods of choroidal neovascularization detection using optical coherence tomography angiography. U.S. Patent Application 15/080,498.
- [56] Yang, Q., Zhang, J., Nozato, K., Saito, K., Williams, D. R., Roorda, A., & Rossi, E. A. (2014). Closed-loop optical stabilization and digital image registration in adaptive optics scanning light ophthalmoscopy. *Biomedical optics express*, 5(9), 3174-3191.
- [57] Zaki, F., Wang, Y., Su, H., Yuan, X., & Liu, X. (2017). Noise adaptive wavelet thresholding for speckle noise removal in optical coherence tomography. *Biomedical Optics Express*, 8(5), 2720-2731.

- [58] Jahromi, M. K., Kafieh, R., Rabbani, H., Dehnavi, A. M., Peyman, A., Hajizadeh, F., & Ommani, M. (2014), "An automatic algorithm for segmentation of the boundaries of corneal layers in optical coherence tomography images using gaussian mixture model". *Journal of Medical Signals and Sensors*, 4(3), 171–180.
- [59] Lezama, J., Mukherjee, D., McNabb, R. P., Sapiro, G., Kuo, A. N., & Farsiu, S. (2016). Segmentation guided registration of wide field-of-view retinal optical coherence tomography volumes. *Biomedical optics express*, 7(12), 4827-4846.
- [60] Dascal, L., & Winkler, I. (2016). U.S. Patent Application No. 15/355,921.
- [61] Baghaie, A., Yu, Z., & D'Souza, R. M. (2017). Involuntary eye motion correction in retinal optical coherence tomography: Hardware or software solution?. *Medical image analysis*, 37, 129-145.
- [62] T. (. L. Deserno, "Medizinische Bildverarbeitung," in *Kramme R. (eds) Informationsmanagement und Kommunikation in der Medizin*, Berlin, Heidelberg, Springer, 2017.
- [63] Handels, H. (2009). *Medizinische Bildverarbeitung: Bildanalyse, Mustererkennung und Visualisierung für die computergestützte ärztliche Diagnostik und Therapie*. Springer-Verlag.
- [64] Ginner, L., Blatter, C., Fechtig, D., Schmoll, T., Gröschl, M. and Leitgeb, R. (2014). Wide-Field OCT Angiography at 400 KHz Utilizing Spectral Splitting. *Photonics*, 1(4), pp.369-379.
- [65] Chiu, S. J., Li, X. T., Nicholas, P., Toth, C. A., Izatt, J. A., & Farsiu, S. (2010). Automatic segmentation of seven retinal layers in SDOCT images congruent with expert manual segmentation. *Optics express*, 18(18), 19413-19428.
- [66] "TU München," [Online]. Available: [https://www-m9.ma.tum.de/graph-algorithms/spp-dijkstra/index\\_de.html](https://www-m9.ma.tum.de/graph-algorithms/spp-dijkstra/index_de.html). [Accessed 30 11 2017].
- [67] "Game Theory lab, CSA," 01 12 2017. [Online]. Available: <http://lcm.csa.iisc.ernet.in/dsa/node162.html>. [Accessed 30 11 2017].
- [68] Gonzalez, R. C., & Woods, R. E. (1992). *Digital image processing (Vol. 3)*. Reading: Addison-wesley, 3rd ed. ed., p. 954.
- [69] Oliveira, F. D., Haas, H. L., Gomes, J. G. R., & Petraglia, A. (2013). CMOS imager with focal-plane analog image compression combining DPCM and VQ. *IEEE Transactions on Circuits and Systems I: Regular Papers*, 60(5), 1331-1344.
- [70] "Natural Resources Canada," [Online]. Available: <http://www.nrcan.gc.ca/node/14641>.
- [71] Zhu, Y., & Huang, C. (2012). An improved median filtering algorithm for image noise reduction. *Physics Procedia*, 25, 609-616.
- [72] Lin Yin, Ruikang Yang, Gabbouj and Neuvo (1996). Weighted median filters: a tutorial. *IEEE Transactions on Circuits and Systems II: Analog and Digital Signal Processing*, 43(3), pp.157-192.

- [73] Griffith, D. A. (2013). *Spatial autocorrelation and spatial filtering: gaining understanding through theory and scientific visualization*. Springer Science & Business Media.
- [74] "THE UNIVERSITY OF EDINBURGH," [Online]. Available: <https://homepages.inf.ed.ac.uk/rbf/HIPR2/median.htm>.
- [75] Shapiro, L. and Stockman, G. (2001). *Computer vision*. Upper Saddle River, New Jersey: Prentice Hall, 279-325.
- [76] "Slideshare/FFT," [Online]. Available: <https://www.slideshare.net/Forward2025/radar-2009-a-3-review-of-signals-systems-and-dsp-58231358>. [Accessed 29 09 2017].
- [77] Masland, R. H. (2001). The fundamental plan of the retina. *Nature neuroscience*, 4(9), 877-886.
- [78] Park, J. J., Soetikno, B. T., & Fawzi, A. A. (2016). Characterization of the middle capillary plexus using optical coherence tomography angiography in healthy and diabetic eyes. *Retina*, 36(11), 2039-2050.
- [79] Niu, S., Chen, Q., de Sisternes, L., Rubin, D. L., Zhang, W., & Liu, Q. (2014). Automated retinal layers segmentation in SD-OCT images using dual-gradient and spatial correlation smoothness constraint. *Computers in biology and medicine*, 54, 116-128.
- [80] Wylęgała, A., Teper, S., Dobrowolski, D., & Wylęgała, E. (2016). Optical coherence angiography: A review. *Medicine*, 95(41).